Role of emission sources and atmospheric sink on the seasonal cycle of CH$_4$ and δ^{13}-CH$_4$: analysis based on the atmospheric chemistry transport model TM5

Vilma Kangasaho[1], Aki Tsuruta[1], Leif Backman[1], Pyry Mäkinen[2], Sander Houweling[3,4], Arjo Segers[5], Maarten Krol[6,7], Ed Dlugokencky[8], Sylvia Michel[9], James White[9], and Tuula Aalto[1]

[1]Finnish Meteorological Institute, P.O. Box.503, FI-00101, Helsinki, Finland
[2]Aalto University, Finland
[3]SRON Netherlands Institute for Space Research, the Netherlands
[4]Vrije Universiteit Amsterdam, the Netherlands
[5]Netherlands Organisation for Applied Scientific Research (TNO), Utrecht, the Netherlandss
[6]Wageningen University & Research, Meteorology and Air Quality, the Netherlands
[7]IMAU, Utrecht University, the Netherlands
[8]NOAA Global Monitoring Laboratory (GML), USA
[9]NSTAAR, University of Colorado, USA

Correspondence: Vilma Kangasaho (vilma.kangasaho@fmi.fi)

Abstract. This study investigates the contribution of different CH$_4$ sources to the seasonal cycle of δ^{13}C during years 2000–2012 using the TM5 atmospheric transport model. The seasonal cycles of anthropogenic emissions from two versions of the EDGAR inventories, v4.3.2 and v5.0 are examined. Those includes emissions from Enteric Fermentation and Manure Management (EFMM), rice cultivation and residential sources. Those from wetlands obtained from LPX-Bern v1.4 are also

5   examined in addition to other sources such as fires and ocean sources. We use spatially varying isotopic source signatures for EFMM, coal, oil and gas, wetlands, fires and geological emission and for other sources a global uniform value.

We analysed the results as zonal means for 30° latitudinal bands. Seasonal cycles of δ^{13}C are found to be an inverse of CH$_4$ cycles in general, with a peak-to-peak amplitude of 0.07–0.26 ‰. However, due to emissions, the phase ellipses do not form straight lines, and the anti-correlations between CH$_4$ and δ^{13}C are weaker (-0.35 to -0.91) in north of 30° S. We found that

10 wetland emissions are the dominant driver in the δ^{13}C seasonal cycle in the Northern Hemisphere and Tropics, such that the timing of δ^{13}C seasonal minimum is shifted by ∼90 days in 60° N–90° N from the end of the year to the beginning of the year when seasonality of wetland emissions is removed. The results also showed that in the Southern Hemisphere Tropics, emissions from fires contribute to the enrichment of δ^{13}C in July–October. In addition, we also compared the results against observations from the South Pole, Antarctica, Alert, Nunavut, Canada and Niwot Ridge, Colorado, USA. In light of this

15 research, comparison to the observation showed that the seasonal cycle of EFMM emissions in EDGAR v5.0 inventory is more realistic than in v4.3.2. In addition, the comparison at Alert showed that modelled δ^{13}C amplitude was approximately half of the observations, mainly because the model could not reproduce the strong depletion in autumn. This indicates that CH$_4$ emission magnitude and seasonal cycle of wetlands may need to be revised. Results from Niwot Ridge indicate that in addition to biogenic emissions, the proportion of biogenic to fossil based emissions may need to be revised.

1 Introduction

Methane (CH_4) is a greenhouse gas of which the abundance is severely perturbed by anthropogenic activities. It causes 28 times more radiative forcing than equal emissions of CO_2 when integrated over 100 years. The abundance of CH_4 in the atmosphere has more than doubled since the pre-industrial times (Hartmann et al., 2013). CH_4 is emitted to the atmosphere from thermogenic, pyrogenic, and biogenic sources, which can be of natural or anthropogenic in origin (Saunois et al., 2020). Most of the seasonal cycle in CH_4 emission is driven by the pyrogenic and biogenic sources, such as biomass burning, wetlands and rice cultivation (Crippa et al., 2020; Bergamaschi et al., 2018; Bloom et al., 2017; Basso et al., 2016; Giglio et al., 2013). The processes are highly dependent on climatological and meteorological conditions, such as temperature and precipitation, and cultivation cycles. In contrast, thermogenic sources, such as fossil fuel extraction and distribution, have little month-to-month variation, although winter emissions may be greater in some regions due to consumption of natural gas for heating (Crippa et al., 2020). Likewise, instantaneous perturbations in emissions may occur due to blowout events from natural gas wells (Kuze et al., 2020; Pandey et al., 2019).

Seasonal variations in wetland CH_4 emissions have been much studied by site-level measurements (e.g. Delwiche et al., 2021; Villarreal and Vargas, 2021), process-based land surface ecosystem models (e.g. Parker et al., 2020), and atmospheric inversions (e.g. Xu et al., 2016; Zhang et al., 2021), but there are still large uncertainties in the magnitude and timing of maximum emissions on continental to regional scales (Warwick et al., 2016; Bergamaschi et al., 2018; Tsuruta et al., 2019). Anthropogenic based thermogenic and biogenic CH_4 emission cycles mainly depend on political decisions. Although some countries report emission magnitudes to e.g. UNFCCC, often only annual values are reported, and emissions from e.g. rice paddies may not properly consider e.g. temperature dependencies and soil properties (Yan et al., 2009). In addition, emissions from livestock (e.g. enteric fermentation and manure management) may have seasonal cycles depending on temperature (Elsgaard et al., 2016). However, again, such information is often not included in the reported emissions, and only few global inventories take the seasonal changes from this sector into account (Crippa et al., 2020, and references therein).

CH_4 has two stable carbon isotopes, ^{12}C and ^{13}C, and hydrogen isotopes, ^{1}H and ^{2}H. For the carbon isotopes, their process specific isotopic signatures ($^{13}C/^{12}C$ ratio compared to a reference, denoted as $\delta^{13}C$) depend on processes that produce CH_4 (Nisbet et al., 2016). Generally, emissions with pyrogenic origin are most enriched in ^{13}C, followed by the thermogenic sources. Sources from biogenic origin are most depleted in ^{13}C (e.g. Nisbet et al., 2016; Sherwood et al., 2017). Such information has shown to be useful in quantifying CH_4 source distributions (Schwietzke et al., 2016; Thompson et al., 2018; Monteil et al., 2011; Lan et al., 2021), in addition to CH_4-only atmospheric inversions, which estimates total CH_4 budgets (e.g. Saunois et al., 2020; Houweling et al., 2014). However, the CH_4 flux information derived using the information from isotopic measurements still have large uncertainty as the isotopic measurements are still limited in both spatial and temporal coverage, and partly overlapping signatures makes source division uncertain (Schwietzke et al., 2016). On top of that, the isotopic signature of emissions can vary significantly by locations due to differences in production processes, types of origin or methanogeneisis (Ganesan et al., 2018; Feinberg et al., 2018; Etiope et al., 2019; Brownlow et al., 2017). Ganesan et al. (2018) also warned that the emission quantification, including its seasonality, may lead to erroneous results without fully incorporating detailed spatial

Atmospheric
Chemistry
and Physics
Discussions

Open Access
EGU

information of the isotopic signatures. In addition, the fractionation factor of OH vary between studies (Saueressig et al., 2001;
Cantrell et al., 1990). The role and magnitude of tropospheric Cl sink is also uncertain ranging from 13–37 Tg CH$_4$ yr^{-1} (Allan
et al., 2007) to 12—13 Tg CH$_4$ yr^{-1} (Hossaini et al., 2016) to even smaller estimates (Gromov et al., 2018)].

The seasonal cycle of δ^{13}C is determined by atmospheric sinks and emissions. Sinks enrich the atmosphere in the ^{13}CH$_4$,
and they have a strong seasonality due to their kinetic isotopic effect (KIE). In general, the δ^{13}C cycle is mirroring the CH$_4$
cycle in high southern latitudes, where the effect of emissions are small (Saueressig et al., 2001; Bergamaschi et al., 1996).
However, the δ^{13}C cycle is known to be affected by the seasonal variations in emissions, where majority of the emissions
deplete the atmosphere in ^{13}CH$_4$. Therefore, the δ^{13}C cycles do not correlate well with the atmospheric CH$_4$ cycles, especially
in the Northern Hemisphere (NH) (Allan et al., 2001b; Bergamaschi et al., 2000; Tyler et al., 2007). These studies found
that the δ^{13}C seasonal cycle reaches its maximum approximately two months later than CH$_4$ reaches its minimum in the NH.
Studies using inverse transport modelling indicate that the weak negative correlations and phase shifts are strongly influenced
by wetlands in the northern high latitudes and biomass burning in the Tropics (Bergamaschi et al., 2000; Allan et al., 2001b;
Fujita et al., 2018; Warwick et al., 2016).

In this study, we examine the average δ^{13}C seasonal cycle for the time period 2000–2012, and CH$_4$ source and sink contri-
butions at 30° latitudinal bands based on the TM5 global atmospheric transport model. We estimate atmospheric CH$_4$ and δ^{13}C
cycles using the most recent isotopic signatures published, and five sectoral emission fields with different seasonality, includ-
ing those from the anthropogenic sources, and examine the differences in the combined CH$_4$ and δ^{13}C cycles. In addition, we
evaluate the seasonal cycle in anthropogenic emission by comparing model estimates derived using the two recent versions of
EDGAR inventory, v4.3.2 and v5.0, against observations from the National Oceanic and Atmospheric Administration Global
Monitoring Laboratory (NOAA/GML) and the Institute of Arctic and Alpine Research (INSTAAR).

2 Materials and Methods

2.1 TM5 atmospheric chemistry transport model

TM5 (Krol et al., 2005) is a global Eulerian atmospheric chemistry transport model. It is driven by ECMWF ERA-Interm
meteorological fields, which for this study is run on a 1° × 1° (latitude × longitude) zoom grid over Europe (up to 74° N)
embedded in a 4° × 6° global grid with an intermediate 2° × 3° zoom region (e.g. Tsuruta et al., 2017). Vertically, 25 layers are
used that are a coarsening from the original 60 ERA-Interim layers, and vertical mixing was calculated based on the Gregory
et al. (2000) convection scheme as archived in the ERA-Interim meteorological fields.

In this study, CH$_4$ (incl. ^{12}CH$_4$ and ^{13}CH$_4$) and ^{13}CH$_4$ are transported as two separate tracers, and δ^{13}C−CH$_4$ (δ^{13}C) is
calculated as:

$$\delta^{13}\text{C}-\text{CH}_4 = \left(\frac{(^{13}\text{C}/^{12}\text{C})_{\text{sample}}}{R_{\text{std}}} - 1 \right) \times 1000, \tag{1}$$

where $R_{\text{std}} = 0.0112372$ is the isotopic (^{13}C and ^{12}C) ratio of the standard, Vienna Pee-Dee Belemnite (VPDB; de Laeter et al.,
2003).

The atmospheric sink in TM5 includes off-line chemistry; photochemical reactions with OH, Cl, and O(^{1}D). The reaction with OH, the largest sink of atmospheric CH_4, is calculated based on Houweling et al. (2014). The monthly variations in OH concentrations are based on Spivakovsky et al. (2000), scaled by 0.92 based on an evaluation using methyl chloroform (Huijnen et al., 2010). The first order loss rates for the reactions with Cl and O(^{1}D) are considered only in stratosphere and are calculated

90 separately, where the rates are based on ECHAM5 general circulation model (Jöckel et al., 2006). No interannual variation of the photochemical sink processes is included in this study, as interannual variations are often assumed to be small for the study period (Zhao et al., 2019; Turner et al., 2019; Rowlinson et al., 2019). Note also that the purpose of the study is to analyse the seasonal cycle, but not trends and interannual variations in the CH_4 and $\delta^{13}C$.

The kinetic isotopic effects (KIE) k($^{12}CH_4$)/k($^{13}CH_4$) = 1.004 is used for $^{13}CH_4$ reaction with OH (Crowley et al., 1999),

95 and 1.066 and 1.013 are used for Cl and O(^{1}D), respectively (Saueressig et al., 2001). In this study, the KIE of total CH_4 is assumed to be the same as for $^{12}CH_4$, i.e. k($^{12}CH_4$)/k($^{13}CH_4$) $\approx$ k(CH_4)/k($^{13}CH_4$).

In addition to the photochemical sinks, we include the sink to dry soils (i.e. a negative flux from atmosphere to soil) in the lowermost layer of TM5. CH_4 is oxidised by bacteria in aerobic mineral soils, and therefore, the sink is dependent on soil moisture, temperature and also soil texture (Spahni et al., 2011). These dependencies lead to the smallest sink in winter and

100 largest sink in summer (Fig. 1). The soil sink can be treated as a pseudo first order reaction $L = k' \cdot [CH_4]$, where $k' = k/h$ and h is the thickness of the lowermost layer. The flux F at the soil surface is $F = k \cdot [CH_4]$. The $^{12}CH_4$ soil sink $F_{\mathrm{soil,12}}$ is taken from the LPX-Bern v1.4 land ecosystem process model (Lienert and Joos, 2018), and varies interannually and monthly. The removal rate of $^{12}CH_4$ is then $L_{\mathrm{soil,12}} = 1/h \cdot F_{\mathrm{soil,12}}$. The removal rate for $^{13}CH_4$ due to the soil sink, $L_{\mathrm{soil,13}}$, is therefore calculated as

$$105 \quad L_{\mathrm{soil,13}} = \frac{F_{\mathrm{soil,12}}}{h \cdot \mathrm{KIE_{soil}}} \times \frac{[^{13}CH_4]}{[^{12}CH_4]} \qquad (2)$$

where $F_{\mathrm{soil,12}}$ is the negative flux of $^{12}CH_4$ at the surface, h is the thickness of the lowermost layer, $[^{12}CH_4]$ and $[^{13}CH_4]$ are the atmospheric concentrations of $^{12}CH_4$ and $^{13}CH_4$, and $\mathrm{KIE_{soil}}$ is assumed to be 1.0177 (Snover and Quay, 2000).

TM5 has been applied to various CH_4 studies, and initial 3-dimensional (3D) CH_4 fields were readily available from e.g. our previous study by Tsuruta et al. (2017). For $^{13}CH_4$, spin-up was needed to create 3D mixing ratio fields that are in approximate

110 steady state. We run 40 years of spin-up (running TM5 using emissions and meteorological fields of year 2000 for 40 times), starting from the converted fields, and based on the emissions and isotopic signatures described in Sections 2.2 and 2.3. The spin-up was started by converting the well-mixed CH_4 fields to $^{13}CH_4$ fields based on Eq. 1, and assuming the average $\delta^{13}C$ in the lowest model layer is -47 ‰ and that of the uppermost layer (95 Pa <) to be -30 ‰. During the spin-up, the spatial distribution and the shapes of vertical profile changed significantly. The value at uppermost layer increased much during the

115 spin-up, and the stratospheric $\delta^{13}C$ increased by ~20 ‰, reaching to approx. -10 ‰ at the end of the spin-up. The exact value of stratospheric $\delta^{13}C$ is unknown due to lack of observations, but -10 ‰ is close to the previous studies (Röckmann et al., 2011; Saueressig et al., 2001). In this study, the focus is in the troposphere and the exact values in stratosphere are not important for our analysis.

2.2 CH$_4$ and ^{13}CH$_4$ flux fields

120 The global CH$_4$ flux fields from anthropogenic and natural sources are taken from inventory and process-based model data (Sections 2.2.1 and 2.2.2). All the fields are pre-processed to a global $1° \times 1°$ grid to match the TM5 model resolution. ^{13}CH$_4$ fluxes are calculated by converting CH$_4$ flux fields using isotopic signature (Table 1) and Eq. 1.

2.2.1 Anthropogenic CH$_4$ flux data

Monthly global anthropogenic emissions are taken from EDGAR inventories (https://edgar.jrc.ec.europa.eu) v4.3.2 (Janssens-
125 Maenhout et al., 2019) and v5.0 (Crippa et al., 2020)). The original resolution is $0.1° \times 0.1°$ (latitude $\times$ longitude) and the inventories are based on the geographical distribution of different activities e.g. energy, agricultural land use and traffic utilising GIS techniques.

The EDGAR database includes emissions from the IPCC 1996 classes 1, 2, 4, 6 and 7 listed in Supplementary Table S1. We categorised these classes into six components: enteric fermentation and manure management (EFMM), landfills and waste
130 water treatment (LWW), rice cultivation (RICE), coal, oil and gas, and residential (Supplementary Table S2). Among these, EFMM, LWW and RICE are anthropogenic biogenic sources, with depleted δ^{13}C isotopic signature, while others are fossil-based sources which are enriched ^{13}CH$_4$ (Fisher et al., 2017). The seasonal cycle of anthropogenic sources are dominated by "anthopogenic" biogenic sources - no significant seasonality is present in the fossil-based sources (Fig. 1).

V4.3.2 is the first EDGAR inventory to include seasonality. It provides monthly values for 2010. We calculated the seasonal
135 cycle for each $1° \times 1°$ grid by applying the 2010 seasonality to other years keeping the same annual totals. For v5.0, monthly values for year 2015 are available, and we applied its seasonality for each grid similarly to the procedure for v4.3.2.

The two EDGAR versions differ significantly in their seasonal cycles of EFMM and RICE (Fig. 1). For the global total EFMM emissions, v4.3.2 has a seasonal maximum in March and a minimum in November, and its average amplitude over 2000–2012 is 7.50 Tg CH$_4$ month^{-1}. In contrast, v5.0 has no seasonal cycle (Fig. 1, Supplementary Table S3). For the global
140 RICE emissions, v4.3.2 has its seasonal maximum in March and its minimum in January and December, and its average amplitude over years 2000–2012 is 2.61 Tg CH$_4$ month^{-1}. The v5.0 RICE emissions has its maximum in August and its minimum in March with an average amplitude over 2000–2012 of 5.51 Tg CH$_4$ month^{-1} (Fig. 1, Supplementary Table S3). The differences in the seasonality is mostly due to the differences: in the spatial distributions in v4.3.2, the seasonality varies over some latitude bands, while in v5.0, it varies by country for which information is available (Crippa et al., 2020). In addition,
145 in v4.3.2 the same temporal profiles is used for all agricultural sectors, which is revised in v5.0 to better correspond each sector separately (Janssens-Maenhout et al., 2019; Crippa et al., 2020)

Annual totals of the two versions also differ slightly. The largest differences are in LWW, where v4.3.2 is lower than v5.0 by 8.2 Tg CH$_4$ year^{-1} compared to v5.0. This gives a global total difference of $\sim$ 7 Tg CH$_4$ year^{-1} between the two versions (global totals for the year 2000 are 292.17 Tg CH$_4$ year^{-1} and 299.05 Tg CH$_4$ year^{-1} for v4.3.2 and v5.0, respectively). Both
150 EDGAR versions have similar trends dominated by increasing trend in EFMM, LWW, coal, and oil and gas (Supplementary
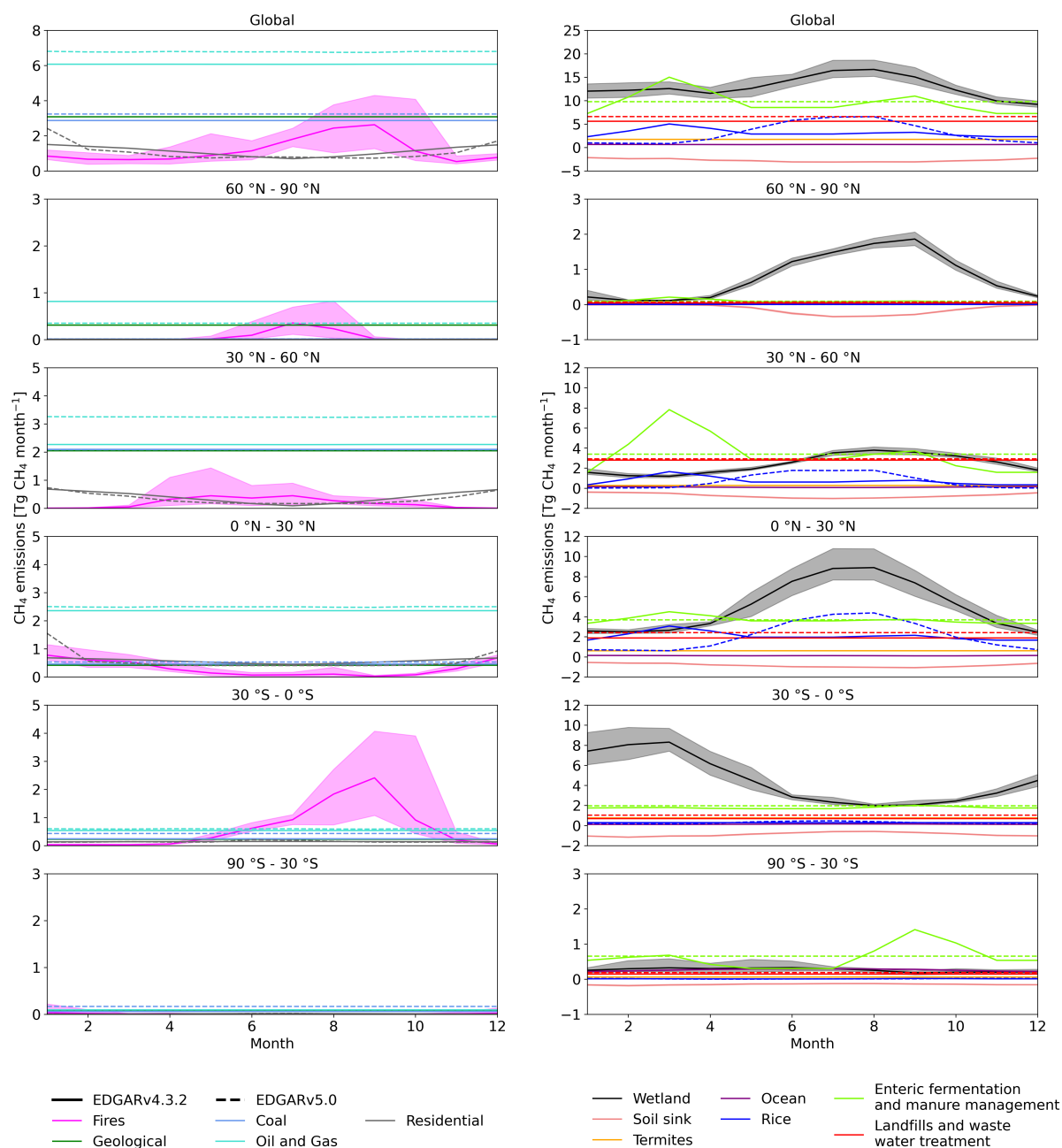
Figure 1. Monthly emission estimates for global (top) and latitudinal zonal totals. The left-hand side panel includes fossil-based emissions and the right-hand side panel emissions from biogenic origin, both natural and anthropogenic. Global emissions (top) are split into 30° latitude bands. Emissions from EDGAR v4.3.2 are for year 2010 and from EDGAR v5.0 for 2015. Natural sources are averages for 2000–2012. Shaded areas show minimum and maximum of the monthly totals over the 2000–2012.

Atmospheric
Chemistry
and Physics
Discussions

Open Access
EGU

Fig. S1). Note however, that this study focuses on the seasonal cycle, and that the analysis of trends will be presented in follow-up studies.

The 2000–2012 average annual total non-biogenic (coal, oil and gas, residential) emissions are similar in both versions, but the biogenic (EFWW, LWW, RICE) emissions are higher in v5.0. The mean ratios (biogenic/non-biogenic) are 1.89

155 (208.17/110.83 Tg CH_4 year^{-1}) and 1.97 (214.97/109.52 Tg CH_4 year^{-1}) in v4.3.2 and v5.0, respectively.

In addition to the two versions of the EDGAR emissions, we created emission fields based on v4.3.2, but removed the seasonal cycle of EFMM by taking annual means. This was used to test the effect of the seasonally varying EFMM emissions, which was largest in v4.3.2, but absent in v5.0.

2.2.2 Natural CH_4 flux data

160 Natural sources include those from wetlands, biomass burning, open ocean, termites and geological sources. Among these sectors, emissions from wetlands and termites are biogenic sources with depleted $\delta^{13}C$ values, while others are considered non-biogenic with more enriched $\delta^{13}C$ values (Table 1). Monthly wetland emissions are taken from the process-based land ecosystem model LPX-Bern v1.4 (Lienert and Joos, 2018), which is a dynamic vegetation model that estimates fluxes for wetlands. Wetland emissions have the largest seasonal cycle amplitude among all source categories (Fig. 1) with a global

165 average amplitude of 8.10 Tg CH_4 month^{-1} averaged over 2000–2012. The seasonal minimum occurs in winter, and the maximum in summer, i.e. July - August in the NH and January–February in the Southern Hemisphere (SH) (Fig. 1).

Monthly biomass burning emissions are taken from GFED v4.2 (Giglio et al., 2013). Biomass burning emissions vary strongly from year to year, and the amplitude in the seasonal cycle varies much by year and locations (Fig. 1). For the global total, the average amplitude during 2000–2012 is 2.49 CH_4 Tg month^{-1}, and the maximum and minimum amplitudes during

170 2000–2012 are 3.95 and 1.07 CH_4 Tg month^{-1}, respectively. Monthly emissions from open ocean were calculated assuming a supersaturation of CH_4 in the seawater of 1.3 (Lambert and Schmidt, 1993). The sea-air flux of methane was calculated using ECMWF ERA-interim data (Dee et al., 2011) of sea surface temperature, sea ice concentration, surface pressure and wind speed (Tsuruta et al., 2017). The amplitude of its seasonal cycle is relatively small, with a global average of 0.08 CH_4 Tg month^{-1} during 2000–2012. For termites and geological sources, no seasonality is taken into account. The emissions from

175 termites are taken from the VISIT process-based terrestrial ecosystem model (Ito and Inatomi, 2012), and gridded emission maps by Etiope et al. (2019) are used for geological sources. Geological emissions by Etiope et al. (2019) are scaled down from 37.4 Tg CH_4 year^{-1} to 5 Tg CH_4 year^{-1}, based on Hmiel et al. (2020).

2.3 Isotopic signature

The global $^{13}CH_4$ flux fields were calculated from CH_4 emission fields and Eq. 1 using the isotopic signatures for each source

180 given in Table 1. For LWW, RICE, residential, ocean and termite emissions, the signatures are from Thompson et al. (2018) (mean values), and a single value is applied globally. Spatially varying isotopic signatures are used for EFMM, coal, oil and gas, wetlands, biomass burning and geological emissions. For EFMM, oil and gas, coal and biomass burning, we use the signatures from Feinberg et al. (2018) based on global chemistry-climate simulations of the SOCOL model. For coal, we use the M-COAL

Atmospheric
Chemistry
and Physics
Discussions

Table 1. Isotopic signatures used to convert CH_4 flux fields to $^{13}CH_4$ fields. For values vary globally, ranges of values are shown. Please see Supplementary Fig. S2 for spatial distributions.

Emission source	Signature value
Enteric Fermentation and Manure Management (EFMM)	[-67.9,-54.5][1], -66.8[2]
Landfills and Waste Water Treatment (LWW)	-55.6[2]
Rice (RICE)	-62.1[2]
Coal	[-64.1, -36.1][1], -40[2]
Oil and Gas	[-56.6, -29.1][1], -40[2]
Residential	-40[2]
Wetlands	[-74.9, -50][3], -61.3[2]
Fires	[-25, -12][1], -22.2[2]
Ocean	-47[2]
Termites	-65.2[2]
Geological	[-68, -24.3][4], -40[2]

[1] Feinberg et al. (2018),[2] Thompson et al. (2018), [3] Ganesan et al. (2018), [4] Etiope et al. (2019)

version presented by Feinberg et al. (2018). For geological and wetland emissions, the signatures from Etiope et al. (2019) and

185   Ganesan et al. (2018) are used, respectively. The Ganesan et al. (2018) values are based on observations characterising wetland ecosystems. The isotopic signatures from Feinberg et al. (2018) were originally given on in T42 resolution, and emission from wetlands on $0.5° \times 0.5°$. We converted those to $1° \times 1°$ resolution by choosing the closest coordinate value and by taking simple grid averages, respectively. Grid cells with missing data are filled with mean values from Thompson et al. (2018). The applied isotopic signatures do not have seasonal or inter-annual variations. This is appropriate if we assume that the spatial

190   distribution of the sources does not change, but only the magnitude.

We acknowledge that there are some differences in the spatial distributions of emissions used in e.g. Feinberg et al. (2018) against the EDGAR versions and Ganesan et al. (2018) against LPX-Bern v1.4, i.e. the signatures are not custom-made for our emission fields. Therefore, the corresponding signature values may not be appropriate in all grid cells. However, considering the large range in source signatures (Schwietzke et al., 2016; Nisbet et al., 2016; Sherwood et al., 2017), we assume that our

195   values are a good approximation for examining the cause of $\delta^{13}C$ seasonal cycle.

2.3.1 Isotopic signatures in spin-up simulations

There are large uncertainties in the magnitude and spatial distribution of the isotopic signature, and therefore, we performed several spin-up simulations with slightly different isotopic signature to examine the effect in $\delta^{13}C$ seasonal cycle. We first examined the filled values (grids with no initial value assigned) by applying the values from Monteil et al. (2011) and Thompson

200   et al. (2018). We also used a weighted mean value, which lead to less negative values of $\delta^{13}C$, i.e. more enriched with $^{13}CH_4$ for most of the sources. In contrary to expectation, the different filling values did not affect the seasonality of $\delta^{13}C$, probably

Table 2. Set of simulations, anthropogenic emission fields used, and emission categories from which seasonal cycle is removed.

Simulation	Anthropogenic emission fields	*Removed seasonal cycle
SIM_E5	EDGAR v5.0	-
SIM_E5_WETNS	EDGAR v5.0	Wetlands
SIM_NS	EDGAR v5.0	All emissions
SIM_E432	EDGAR v4.3.2	-
SIM_E432_EFMMNS	EDGAR v4.3.2	EFMM

due to small emission magnitude in the regions, where the filling values were applied. In addition, we found that the simulated seasonal cycles in $^{13}CH_4$ are rather sensitive to the applied spatial distribution in source signature (e.g. decimal values instead of rounded integers), especially with region of high emission magnitude (Supplementary Fig. S3).

2.4 Atmospheric CH_4 and $\delta^{13}C$ observations

We used CH_4 observations from National Oceanic and Atmospheric Administration - Global Monitoring Laboratory (NOAA/GML) and $\delta^{13}C$ observations from Institute of Arctic and Alpine Research (INSTAAR), University of Colorado Boulder to evaluate the simulation results. In particular, we compared and evaluated model estimates against observations using data from Alert, Nunavut, Canada (ALT; 82.4508° N, 62.5072° W, CH_4: elevation = 185 m a.s.l., intake height = 5 m a.g.), Niwot Ridge, Colorado, USA (NWR; 40.0531° N, 105.5864° W, elevation = 3523 m a.s.l., intake height = 3 m a.g.) and South Pole, Antarctica (SPO; 89.98° S, 24.8° W, elevation = 2810 m a.s.l., intake height = 3–11.3 m a.g.). SPO is an optimal place to evaluate the seasonal cycle of background levels of CH_4, and there are no major CH_4 sources nearby. In contrast, NWR is located in the front range of the Colorado Rockies, and mainly measures well-mixed background air. NWR measurements influenced by strong anthropogenic sources are filtered out. Finally, ALT is located far away from anthropogenic sources, and samples air that is more influenced by distant wetland fluxes, whereas SPO is located far away from all sources both natural and biogenic. Note, none of the stations are located in the TM5 1° × 1° zoom region, and the model values are sampled from 4° × 6° grid using 3D linear interpolation.

For comparison, observations from 2002–2012 are used. The first two years were omitted from the analysis to be comparable to the modelled seasonality (see Section 3.1.1). To obtain detrended data we used curve fitting methods by Thoning et al. (1989). We calculated the short term smoothed curve and the trend curve. The detrended seasonal cycle is obtained by subtracting the trend curve from the smooth curve. The $\delta^{13}C$ observations from 2007 onward have different trends than those in 2002–2006 (Nisbet et al., 2019). However, using the method from Thoning et al. (1989) we can compare years with different trends.

2.5 Simulation setups

We carried out five TM5 simulations using different input emission fields for 2000–2012 (Table 2). The end year 2012 is the last year for which the EDGAR 4.3.2 data is available. To examine the effect of the seasonal cycle in emissions, we used two

Atmospheric
Chemistry
and Physics
Discussions

versions of the EDGAR inventory, v5.0 (SIM_E5) and v4.3.2 (SIM_E432), and those without EFMM seasonal cycle in v4.3.2 (SIM_E432_EFMMNS). In addition, we examined the seasonal cycle in wetland emission by using annual mean emissions (SIM_E5_WETNS) instead of a seasonal cycle. We further examined the δ^{13}C seasonal cycle exclusively caused by the CH$_4$ sinks by removing the seasonal cycle of all emission sources (SIM_NS).

230 ## 3   Results

3.1   Zonal means near the surface

Detrended zonal mean atmospheric CH$_4$ (ΔCH$_4$) and δ^{13}C ($\Delta\delta^{13}$C) values from the simulations are compared at 30° latitudinal bands. The trend and smoothed fit are calculated for 2000–2012 from the lowest five layers of TM5 (up to approx. 850 hPa) based on Thoning et al. (1989), and the detrended smoothed fit is averaged over 2002-2012 to examine the seasonal cycle. Note

235   that we found that it takes approximately two years for the seasonal cycle of the lower atmosphere to stabilise by changing emission fields to those used in spin-up (Supplementary Fig. S5). Therefore, in order to remove the effect of initial state, the first two years of the forward simulations are omitted from the analysis. In this section, we focus on the seasonal cycle in $\Delta\delta^{13}$C and its relation to ΔCH$_4$ cycle in Section 3.1.2, as CH$_4$ cycle has been discussed extensively in previous studies (e.g. Dlugokencky et al., 1997; Javadinejad et al., 2019; Kivimäki et al., 2019; Khalil and Rasmussen, 1983).

240   We acknowledge that the δ^{13}C cycles are affected by local sources, and can vary spatially at smaller resolution than 30° latitudinal bands (Hein et al., 1997; Allan et al., 2001b; Warwick et al., 2016; Fujita et al., 2018; Bergamaschi et al., 2000). In addition, tropical meteorological dynamics such as the positions of the Intertropical Convergence Zone and the South Pacific Convergence Zone affect the seasonality of CH$_4$ and δ^{13}C, and these variations can not be distinguished by using 30° latitudinal means (Lowe et al., 2004).

245 ### 3.1.1   Peak-to-peak amplitude and shape of δ^{13}C seasonal cycle

Generally, the seasonal cycle of $\Delta\delta^{13}$C mirrors the seasonal cycle of ΔCH$_4$, such that δ^{13}C has seasonal minimum in winter and maximum in summer in the NH, and vice versa for the SH (Fig. 2). Seasonal variations of both CH$_4$ and δ^{13}C are larger in the NH than in the SH, mostly because the major emission sources are located in the NH. The seasonal cycle amplitude for ΔCH$_4$ in our model is the largest in the NH Tropics EQ–30° N (49.7 ppb, SIM_E5), while that for $\Delta\delta^{13}$C is the largest at 60° N–90°

250   N (0.26 ‰, SIM_E5). The smallest amplitude is found in the SH Tropics (30° S–EQ) for both ΔCH$_4$ and $\Delta\delta^{13}$C, with 15.1 ppb and 0.07 ‰, respectively (SIM_E5). This is well in line with previous studies (e.g. Allan et al., 2001a; Tyler et al., 1994a). The $\Delta\delta^{13}$C seasonal cycle amplitude in 90°S–60°S approximately half of 60° N–90° N, while it is 25 % smaller in ΔCH$_4$. Wetland emissions are the largest natural source of CH$_4$ and have the largest seasonal cycle among all emission categories, with the highest emissions during summer and autumn (in respective hemispheric seasons) (Fig. 1). Wetlands are biogenic sources,

255   with depleted isotopic signatures (Section 2.3), i.e. increases in wetland emissions will result in decreases in δ^{13}C. When the seasonality of wetland emissions is removed (SIM_E5_WETNS), the largest seasonal cycle amplitudes are found in 60° N–90°

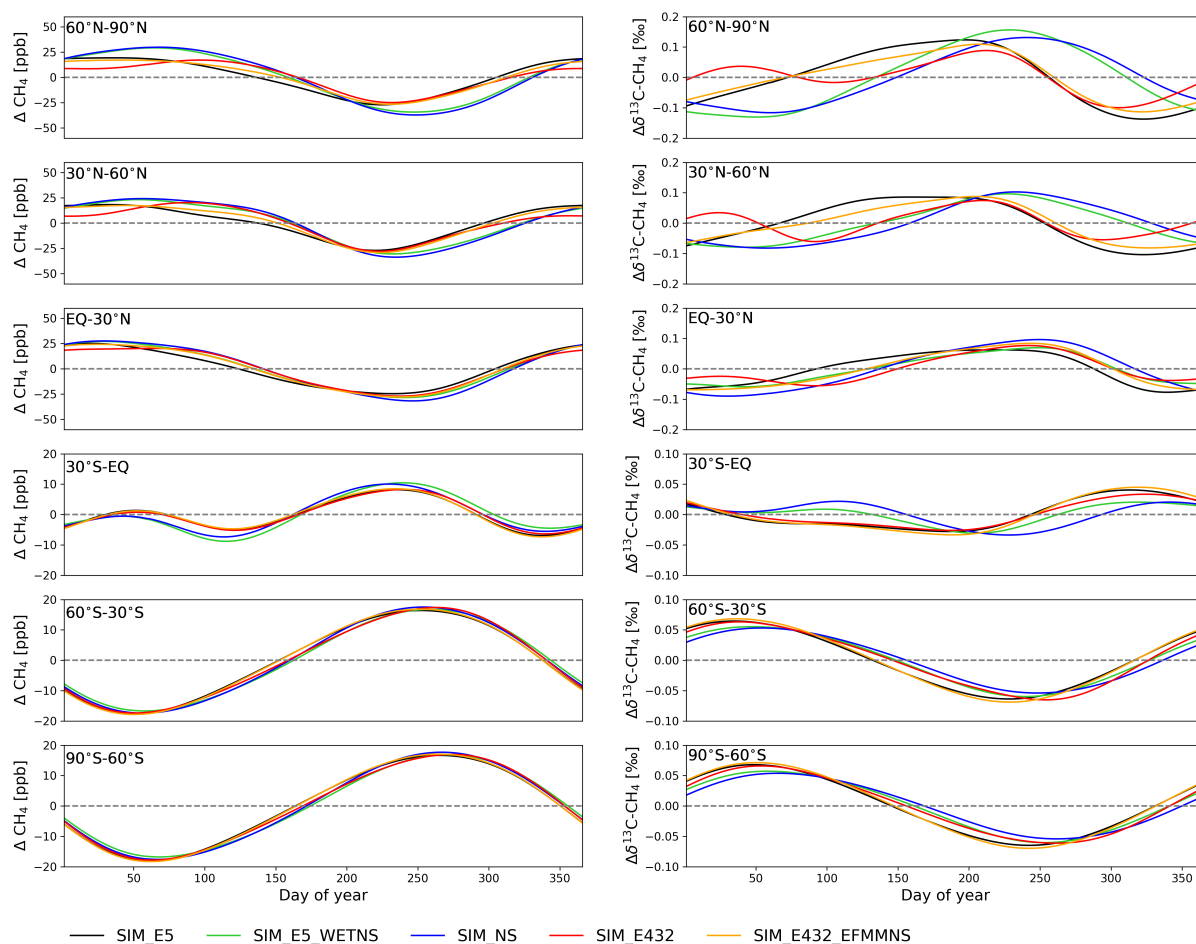**Figure 2.** Detrended zonal mean averages for CH_4 (left) and $\delta^{13}C$ (right) from model simulations, averaged over 2002–2012 and the lowest 5 layers. Note differences in y-axis for the Northern and Southern Hemispheres.

N for both ΔCH_4 (63.4 ppb) and $\Delta\delta^{13}C$ (0.29 ‰), which is an increase of 28 % and 10 % compared to SIM_E5, respectively. The smallest amplitudes are again found in 30° S–EQ (19.3 ppb and 0.05 ‰). In that latitude band, the $\Delta\delta^{13}C$ amplitude decreased 25 % compared to SIM_E5, and that of ΔCH_4 shows an 28 % increase. Generally in the NH, the amplitude of ΔCH_4

260 increased (12–37 %), while the $\Delta\delta^{13}C$ amplitudes decreased slightly at all latitudes (7–25 %), except for 60°N–90°N, which increased by 10 %. Although wetland emissions have the largest seasonal cycle amplitude in the Tropics (Fig. 1), removing the seasonal cycle resulted in an increase in the ΔCH_4 amplitudes because a compensating effect is eliminated: normally wetland emissions increases (decreases) at the same time as the oxidation capacity increases (decreases). In contrast, the $\Delta\delta^{13}C$ amplitude at 60° N–90° N increased because normally wetland emissions decreased (increased) when OH concentrations are

265 high (low). The results also indicate that the contribution of the wetland emissions to the $\Delta\delta^{13}C$ amplitude is equally strong in mid-latitudes in both hemispheres (10 % in 60° S–30° S and 7 % in 30° N–60° N), while the effect on ΔCH_4 is much stronger

Atmospheric
Chemistry
and Physics
Discussions
Open Access
EGU

in the NH (19 %, 30° N–60° N) compared to the SH (≤ -2 %, 30° S–60° S). The largest differences in the shapes of the $\Delta\delta^{13}$C seasonal cycles between SIM_E5_WETNS and SIM_E5 are found at latitudes north of 30° S (Fig. 2). In the NH, $\Delta\delta^{13}$C in SIM_E5 is increasing in spring towards autumn, while it is decreasing in SIM_E5_WETNS in spring. The depletion of $\Delta\delta^{13}$C

270   in autumn is more gradual in SIM_E5_WETNS, and continuously decreasing towards winter. The time when the seasonal minimum occurs is significantly shifted from the end of the year to the beginning of the year by 69–93 days in the NH. The changes in phase of peak maxima are smaller (6–32 days), except for the band 30° N–60° N, which is shifted towards autumn by 67 days. In 30° S–EQ, $\Delta\delta^{13}$C is decreasing in the beginning of year in SIM_E5, while it is increasing in SIM_E5_WETNS. This creates two maxima peaks in SIM_E5_WETNS; one on DOY = 98 and another on DOY = 319, although the latter peak

275   is more than two times larger (Fig. 2).In south of 30° S, the differences are small, but the timing of the minima and maxima peaks are consistently shifted later by ~9–12 days. Although wetland emissions in the NH increase in spring, the effect on $\Delta\delta^{13}$C is seen in autumn (lag-effect). When the effect of the emissions is removed, the $\Delta\delta^{13}$C cycle closer follows the cycle in atmospheric oxidation. When the seasonal cycles of all emissions (SIM_NS) are removed, i.e. the seasonality is only driven by the atmospheric and soil sinks (see Sections 2.1 and 2.2), the seasonal cycles of ΔCH$_4$ and $\Delta\delta^{13}$C are affected similarly to

280   SIM_E5_WETNS (Fig. 2). This indicates that wetlands are the dominant source driving the $\Delta\delta^{13}$C seasonal cycle, apart from sinks. Similarly to SIM_E5_WETNS, $\Delta\delta^{13}$C in the NH decreased in spring and gradually decreased in autumn. The $\Delta\delta^{13}$C seasonal cycle amplitude in SIM_NS is smaller compared to SIM_E5 at all latitudes, except for EQ–30° N where the SIM_NS amplitude (0.19 ‰) is the largest among all simulations. The timing of minima shift to later date compared to SIM_E5_WETNS in general (Fig. 2). The most notable differences are found in 30°S–EQ, where the maximum in SIM_NS occurs on DOY =

285   108, while all other simulations have maxima between DOY 313 and 324. Together with the results from SIM_E5_WETNS, this indicates that wetland emissions contribute to the depletion of $\Delta\delta^{13}$C in the beginning of the year in this latitude band, and other emissions contribute to enrichment of $\Delta\delta^{13}$C at later days. This also indicates that there is only a small lag-effect unlike in the NH; wetland emissions with depleting isotopic signatures are high in January–March, and biomass burning with enriched signature values are high in August–October (Fig. 1). Changing the version of EDGAR inventory (SIM_E432 vs

290   SIM_E5) results in differences in the simulated seasonal cycles, mostly in the NH, as expected. Most notably, NH $\Delta\delta^{13}$C from SIM_E432 shows a clear depletion in spring; it is higher in the beginning of the year, increases for a month or two, and decreases significantly in spring (Fig. 2). The maxima are lower and the depletion in autumn is less significant (Fig. 2), resulting in smaller seasonal cycle amplitudes by 5–29 % in all latitude bands north of 30° S compared to SIM_E5. The seasonal cycle of anthropogenic biogenic sources is driven by EFMM and Rice. Although the emission amplitude of these sources is greater

295   in EDGAR v4.3.2 in 30° N–60° N, the $\Delta\delta^{13}$C amplitude is smaller. This is because EFMM and rice emissions in v4.3.2 are high in spring only one month, while for v5.0 rice emissions are high in summer and remain high for three months (Fig. 1). The minimum in SIM_E432 occur earlier by ~20 days in latitudes 60° N–90° N compared to SIM_E5. For 30° N–60° N, unlike SIM_E5, SIM_E432 has two minima peaks (DOY = 92 and DOY = 294), with spring peak being lower. The largest differences in the timing of the maxima are found in 30° N–60° N, where the SIM_E432 peak occurs 51 days later than that of SIM_E5.

300   It may look as if the effect of anthropogenic biogenic sources comes without much lag-effect, in contrast to wetland emissions (those emissions are larger in spring and lower in winter in EDGAR v4.3.2 than in v5; Fig. 1), but the $\Delta\delta^{13}$C maximum is ~28

% lower in SIM_E432 (north of 30° N). Less EFMM emissions in winter could explain the earlier minimum and higher $\Delta\delta^{13}$C at the end and beginning of the year compared to SIM_E5. Therefore, we suspect that the effect continues for a few months. It is also noted that, the effects of changes in emissions are clearly seen in 60° N–90° N, although anthropogenic emissions and

305   their seasonal cycle in that latitude band are small (Fig. 1). This indicates the strong effect of mid-latitude emissions to the high northern latitudes. When the EFMM seasonal cycle is removed (SIM_E432_EFMMNS), the $\Delta\delta^{13}$C seasonal cycle is closer to that of SIM_E5 than to SIM_E432. The spring depletion is not seen, and magnitude of autumn depletion is similar to SIM_E5 (Fig. 2). However, the maximum is lower and the minimum is higher than in SIM_E5, resulting in 11–15 % smaller amplitudes in latitudes north of 30° N. The amplitudes increase at all other latitudes compared to SIM_E5, but with smaller magnitudes

310   (6–15 %). No significant differences in the timing of minima and maxima are found at other latitudes compared to SIM_E5, except for the timing of the maximum at 30°N–60°N, which is 46 days later. Compared to SIM_E432, the maxima are higher, confirming that the high spring EFMM emissions result in lower $\Delta\delta^{13}$C in halfway of the year (June–August). In addition, the lower winter EFMM emissions contribute to an increase in $\Delta\delta^{13}$C in the beginning of the year, i.e. there is a small lag-effect in how emissions affect $\Delta\delta^{13}$C the cycle.

315   ### 3.1.2   Phase ellipses

The seasonal cycle of $\Delta\delta^{13}$C with respect to the ΔCH$_4$ cycle can be examined with a so-called phase ellipse (Bergamaschi et al., 2000; Allan et al., 2001b). In this study, we examine phase ellipses, where the detrended daily averages of CH$_4$ are plotted against that of δ^{13}C. Fig. 3 shows phase ellipses from the simulations using different emission fields at 30° latitudinal bands. In SIM_NS, the seasonal cycle of the emission components are removed, and the ΔCH$_4$ to $\Delta\delta^{13}$C ratio is only driven

320   by the sinks (atmospheric and soil sinks). The results show high eccentricity of the phase ellipse at south of 60° N, i.e. close to a line, and the correlation $p_0 \approx -1$ and $R^2 \approx 1$ (Fig. 3). The effect of the soil sink is small at these latitudes, so probably the seasonal cycle of $\Delta\delta^{13}$C is preliminarily driven by the atmospheric sinks at these latitudes. Note that the rotation with respect to the DOY on the NH is anticlockwise, and that on the SH clockwise (Fig. 3).

In addition, we examine the timing d (DOY) when the shifted correlations (p_s) between ΔCH$_4$ at time t and $\Delta\delta^{13}$C at time

325   $t+d$ are at minimum and maximum. When there are seasonal cycles only in the atmospheric sinks, we expect $d_{\min} = 0$ and $d_{\max}$ = 366/2 = 183, with $p_s(d_{\min})$ = -1 and $p_s(d_{\max})$ = 1. We use $d_{\min} = d'$ and $d_{\max} = d''$ to denote the specific case when there are no surface emissions or sinks affecting the seasonal cycle. The shifts in $d_{\min}$ and $d_{\max}$ indicate the differences in ΔCH$_4$ and $\Delta\delta^{13}$C cycles, such that the times when $\Delta\delta^{13}$C are in decreasing or increasing phases are earlier or later than phase of ΔCH$_4$.

In SIM_NS, there is no notable shift in d (Supplementary Fig. S4) except for $d_{\max}$ in 30° S–EQ and 60° N–90° N. In 30°

330   S–EQ, the phase ellipse is close to a straight line, with $p_0 \approx -1$ and $R^2 \approx 1$, but $d_{\max}$ = 116, which is 67 days earlier than d''. There are actually two maxima in the shifted correlations, at DOY = 116 and 270, and p_s on these days is ~0.5 (Supplementary Fig. S4). This corresponds mainly to the OH and temperature cycles (OH reaction rate is strongly depended on temperature), where temperature is at maximum in April, and OH concentration in September. In 60°N–90°N, the correlation p_0 = -0.98 and R^2 = 0.96 are not at the minimum or maximum (Fig. 3), and $d_{\max}$ is shifted approx. by -10 days (Supplementary Fig. S4). This

335   is probably due to the effect of the soil sink, which has a larger seasonal cycle amplitude in the NH (1.45 Tg CH$_4$ yr^{-1}) than in
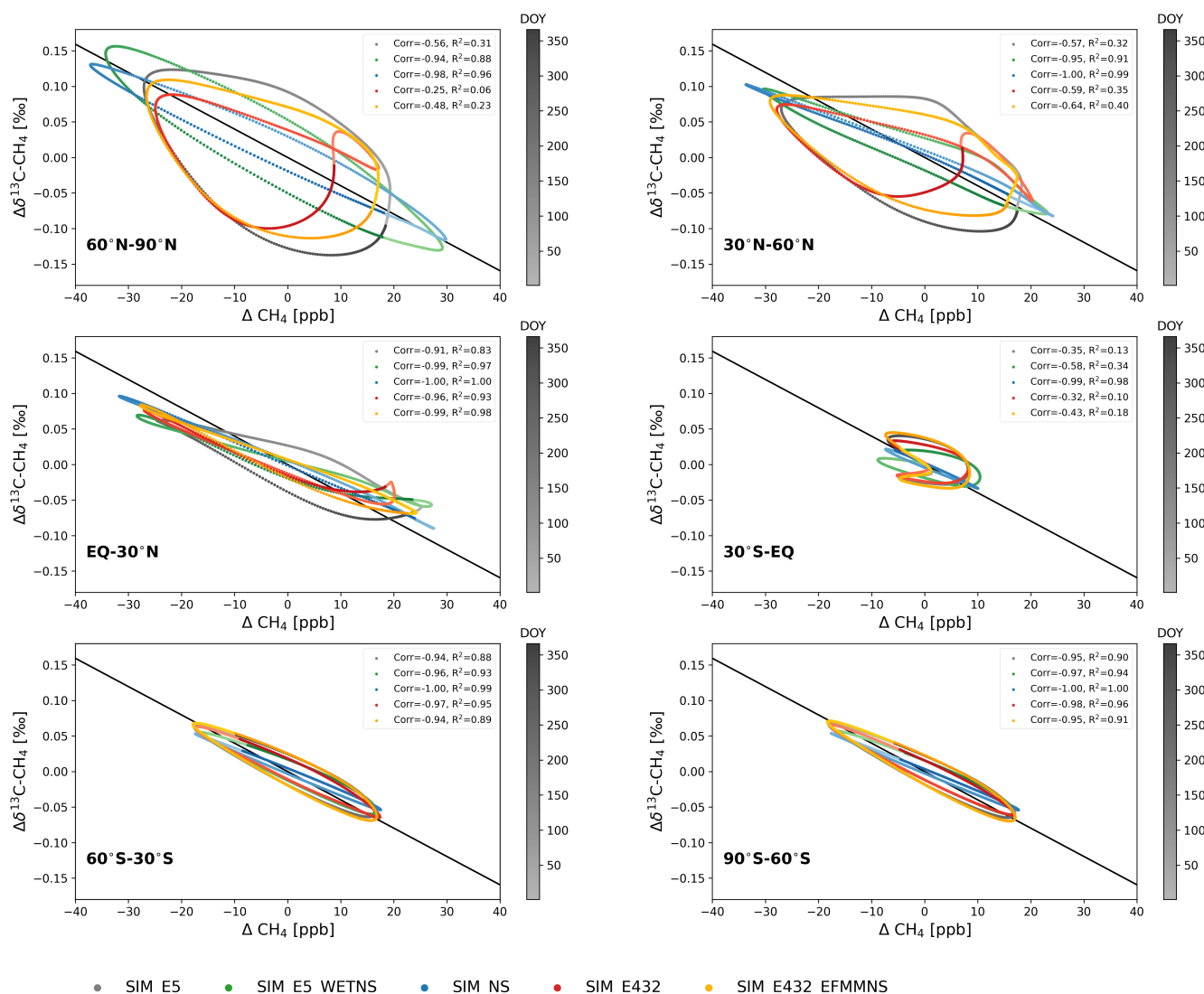
Figure 3. Detrended daily average CH$_4$ against δ^{13}C from the lowest 5 levels over 2002–2012 at 30° latitudinal bands. Colour schemes indicate different simulations, and the colour darkness illustrates day of year (DOY). The lightest colours are DOY = 1 and the darkest DOY = 366. Solid black line is the KIE-line of SIM_NS, and considering only the OH sinks.

14

the SH (0.53 Tg CH$_4$ yr^{-1}) (2000), although the amplitude is not the largest in 60° N–90° N. The soil sink is included only at the lowest layer of TM5, and therefore, transport from lower latitudes and vertical mixing could affect the δ^{13}C seasonal cycle in the upper levels and high latitudes. In addition, the so-called rectifier effect, i.e. correlations between emission and vertical transport, could result in slower ^{12}CH$_4$ transport to the SH during the NH summer when soil sink is strongest. This then gives

340   higher δ^{13}C value in the SH summer. In addition to the phase ellipses, Fig. 3 illustrates the theoretical KIE line when only the OH sink is considered (Allan et al., 2001b). The KIE-line slope is calculated as $\epsilon(1 + \delta_0)$, where ϵ is $(k_{13}/k_{12})_{OH} - 1$ and δ_0 is the mean of $\Delta\delta^{13}$C in SIM_NS. This resulted in KIE of -3.98 ‰. Even in the high SH (90° S–60° S), where the effect of soil sink is small, the phase ellipse from SIM_NS does not exactly follow the KIE-line, indicating the effect of sinks other than OH, i.e. stratospheric Cl, O(^{1}D) and soil sinks, and horizontal long-range and vertical transport.

345   When the emissions' seasonality is included, the ellipses' eccentricity decreases and the shape becomes more like a circle (Fig. 3). The correlation p_0 becomes weaker, R^2 smaller, and d shifts by -97 days the most, indicating the differences in the shape of ΔCH$_4$ and $\Delta\delta^{13}$C seasonal cycles. In SIM_E5, the correlation p_0 is weak (-0.57 to -0.56) and R^2 small (0.31–0.32) in north of 30° N (Fig. 3). The phase ellipses in those latitudes show that 1) both $\Delta\delta^{13}$C and ΔCH$_4$ increase at the end and beginning of the year, i.e. there is no inverse relation in $\Delta\delta^{13}$C and ΔCH$_4$ as in SIM_NS. 2) The relative rate of increase in

350    $\Delta\delta^{13}$C is slower compared to the relative rate of decrease in ΔCH$_4$ in spring, and 3) the relative rate of decrease in $\Delta\delta^{13}$C is faster compared to the relative rate of increase in ΔCH$_4$ in autumn. This effect creates a phase ellipse closer to an oval shape with one axis of symmetry (i.e. an egg-like shape), where the near-circle ellipses (i.e. smaller eccentricity) are formed at end and beginning of the year (short-half), and the other half of the ellipses with higher eccentricity (long-half) (Fig. 3). The $\Delta\delta^{13}$C seasonal cycle amplitude in 60° N–90° N is ~37 % larger than the amplitude at 30° N–60° N (0.26 and 0.19 ‰), creating a

355   larger circle at 60° N–90° N compared to 30° N–60° N (Fig. 3). At latitudes north of 30° N, d_{min} and d_{max} are shifted by approx. -55 and -63 days compared to SIM_NS (Supplementary Fig. S4). As Fig. 2 shows, this indicates that the minimum of $\Delta\delta^{13}$C is ~60 days earlier than the maximum of ΔCH$_4$. In addition, the time of the increasing $\Delta\delta^{13}$C and decreasing CH$_4$ period differ by 39 and 16 days at 30°N–60°N and 60°N–90°N, respectively. This is the effect of changes in the ratio of biogenic and fossil based emissions. At EQ–30°N, the SIM_E5 phase ellipse is closer to a line, especially for the mid-year, compared to that of

360   north of 30° N (Fig. 3). Although eccentricity is smaller for the beginning and the end of the year (short-half), and $\Delta\delta^{13}$C and ΔCH$_4$ are almost always negatively correlated at other days, with d_{min} and d_{max} shifts of only -24 days.

     The SIM_E5 phase ellipse at 30° S–EQ forms an irregular shape, with weak negative correlation $p_0 = -0.35$ and R$^2 = 0.13$ (Fig. 3). As illustrated in Fig. 2, $\Delta\delta^{13}$C decreases in the beginning of the year until approx. DOY = 200, while ΔCH$_4$ has both increasing and decreasing phases during that time. This creates a zigzag line for DOY ≤ 200; 1) close to the SIM_NS line at

365   approx. DOY ≤ 50, 2) perpendicular to the SIM_NS line at approx. 50 < DOY ≤ 120, and 3) horizontal line without much slope at approx. 120 < DOY ≤ 200 (Fig. 3). After approx. DOY ≥ 200, ΔCH$_4$ and $\Delta\delta^{13}$C are anti-correlated, where the slope of the phase ellipse is close to that of SIM_NS. Compared to SIM_NS, the $p_s(d_{max})$ is higher, with shift in d_{max} by -30 days, and the second p_s peak is much smaller (Supplementary Fig. S4). In contrast, the correlation $p_s(d_{min})$ is much weaker than the correlation of SIM_NS. In this latitude band, wetlands and biomass burning are the main contributors to the emission seasonal

370   cycle. Wetland emissions maximize in February–March, while biomass burning maximizes in September–October (Fig. 1).

Thus, although the CH_4 cycle is preliminary driven by OH, differences in the isotopic signatures of the emissions significantly affect the anti-correlation with $\delta^{13}C$ cycle.

At latitudes south of 30° S, the SIM_E5 phase ellipses' eccentricities are very high (Fig. 3) compared to the ellipses found in the NH. The strong correlation $p_0 \leq -0.94$ and $R^2 \geq 0.88$, with shifts in d_{min} and d_{max} by only ~-20 days (Supplementary Fig. S4), indicating that the $\delta^{13}C$ cycle with respect to the CH_4 cycle is preliminary driven by the sinks and little affected by the seasonal cycle of the emissions.

In SIM_E5_WETNS, the phase ellipses are closer to that of SIM_NS than to SIM_E5 at all latitudes except 30° S–EQ (Fig. 3). $\Delta\delta^{13}C$ and ΔCH_4 are mostly anti-correlated in SIM_E5_WETNS, such that the eccentricity of the short- and long-halves of the ellipses do not differ much, and the correlations are strong ($p_0 \leq -0.94$) and R^2 are high (≥ 0.88) at all latitude except 30° S–EQ. This indicates that much of the $\Delta\delta^{13}C$ cycle with respect to ΔCH_4 is driven by wetland emissions. Wetland emission has the largest seasonal cycle amplitude among the emission sources (Fig. 1), and is a main driver for the shape of the $\Delta\delta^{13}C$ cycle (see Section 3.1.1). However, for ΔCH_4, the seasonal cycle is mainly driven by OH, such that the ΔCH_4 cycles do not vary significantly by changes in the emission fields (Fig. 2). At 30° S–EQ the phase ellipse is closer to that of SIM_E5 than to SIM_NS (Fig. 3). The shape of the SIM_E5_WETNS $\Delta\delta^{13}C$ seasonal cycle in the beginning of the year is closest to that of SIM_NS, while it is closer to SIM_E5 in the second half of the year (Fig. 2). However, the $\Delta\delta^{13}C$ increasing and decreasing rates in the beginning of the year (~50 < DOY < 100 and 100 < DOY < 200) are smaller than that of SIM_NS (Fig. 2), creating the phase ellipse offset from the SIM_NS line (Fig. 3). This indicates that, at this latitude band, biomass burning emissions also contribute significantly to the $\Delta\delta^{13}C$ cycle with respect to ΔCH_4 cycle.

The phase ellipses using EDGAR v4.3.2 (SIM_E432, SIM_E432_EFMMNS) generally form circles with smaller radius compared to those of SIM_E5 (Fig. 3) due to smaller $\Delta\delta^{13}C$ peak-to-peak amplitudes (Fig. 2). The shapes of SIM_E432_EFMMNS ellipses at north of 30° N are closer to those of SIM_E5 compared to SIM_E432. This is expected, as the $\Delta\delta^{13}C$ seasonal cycle is close to that of SIM_E5 (Section 3.1.1). The $\Delta\delta^{13}C$ cycle at EQ–30° N is closest to that of SIM_WETNS (Fig. 2), which is also reflected by the phase ellipse being closest to SIM_WETNS. The phase ellipses of SIM_E432 at latitudes north of 30° N are unique, such that they form an extra circle in the beginning of the year (~DOY < 75), outside the oval shape. This results in the weakest anti-correlation ($p_0 = -0.25$) and smallest $R^2 = 0.06$ at 60° N–90° N. These p_0 and R^2 statistics from SIM_E432 are among the smallest at other latitude bands as well.

3.2 Comparison to surface observations

In this analysis, we focus on the evaluation of SIM_E5, SIM_E432 and SIM_E432_EFMM to examine which emission cycle best matches the observed seasonal cycle in $\delta^{13}C$. The peaks and amplitude of the observations are calculated from 30-day moving averages of the detrended data because the variations in the observations are high even after the smooth-fitting (Fig. 4).

At the SPO station, the observations of $\Delta\delta^{13}C$ show a small enrichment in the early months of the year, after which a gradual depletion is observed until SH spring (NH autumn) (Fig. 4). From September to the end of the year, the observations show a gradual enrichment. The amplitude of the mean seasonal cycle over 2002–2012 is 0.15 ‰. The standard deviation of the
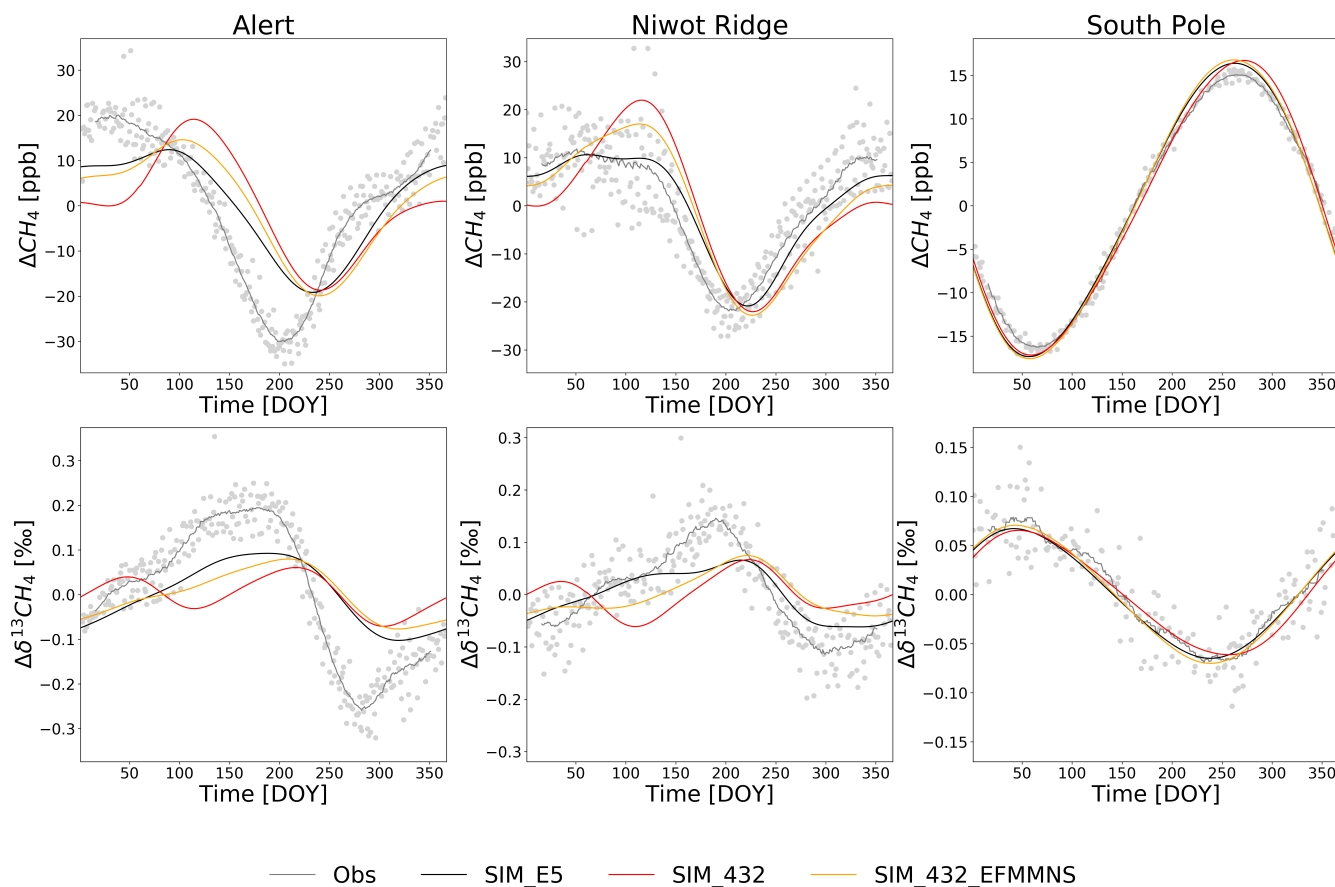
Atmospheric
Chemistry
and Physics
Discussions

Open Access

EGU

Figure 4. Detrended modelled and observed average seasonal cycles during 2002–2012 at Alert, Niwot Ridge, and South Pole. Gray dots are individual detrended observations. Note the differences of the y-axis scales.

detrended observations is $\sigma = 0.048$ ‰. In general, at the SPO station, the model captures the observed seasonal cycle of ΔCH_4 and $\Delta\delta^{13}C$ well. Modelled $\Delta\delta^{13}C$ follows the shape of seasonal cycle well, but the modelled seasonal cycle amplitudes are smaller (0.13–0.14 ‰) compared to the observations (0.15 ‰). For ΔCH_4, modelled amplitudes are 7.7–9.8 % larger than the observations, mainly due to a deeper minimum in the model. As expected, there are no major differences between the simulations in SPO as the site is far from the emissions sources.

At ALT, the observations of $\Delta\delta^{13}C$ show a gradual enrichment until summer (~DOY 200), followed by a strong depletion in autumn (until ~DOY = 260) (Fig. 4). After this depletion, the observations show a gradual enrichment towards the end of the year, continuing to the next summer. The seasonal amplitude in the observations is 0.45 ‰, and model estimates largely underestimate this amplitude by over 50 % (0.13–0.19 ‰). This is mainly because the model is not capturing the strong $\Delta\delta^{13}C$ depletion in summer and autumn (see Section 4 for discussions on reasons). The simulations SIM_E5 and SIM_E432_EFMMN show enrichment in $\Delta\delta^{13}C$ from the beginning of the year until DOY ≈ 200, similar to the observations. However, SIM_E432

shows depletion during DOY ~50 to 120. This suggests that the EFMM emission cycle in EDGAR v4.3.2 causes the depletion in spring, as was shown in the zonal mean estimates (see Section 3.1.1). In addition, the model reaches the $\Delta\delta^{13}$C maximum and minimum ~20 days later than the observations. Modelled ΔCH$_4$ has smaller amplitudes (SIM_E5 31.6 ppb, SIM_E432 37.8 ppb, SIM_E432_EFMM 34.5 ppb) than the observations (50.1 ppb). ΔCH$_4$ is smaller than observed for approx. DOY

420 < 100. Observed ΔCH$_4$ reaches its maximum at approx. DOY = 50 in spring, but the modelled ΔCH$_4$ maximum is 75 days later. The observed ΔCH$_4$ reaches its minimum at approx. DOY = 200, but the modelled ΔCH$_4$ at approx. DOY = 240. In addition, the increase in modelled ΔCH$_4$ remains smaller compared to observations.The shape of the ΔCH$_4$ cycle is closest to the observations in SIM_E5, while the amplitude is closest to SIM_E432. In general, when the modelled $\Delta\delta^{13}$C is lower than the observations, the modelled ΔCH$_4$ is higher than the observations, except during approx. DOY = 25–100 when both

425 $\Delta\delta^{13}$C and ΔCH$_4$ are lower than observations. The differences between the model estimates and observations may be due to smaller magnitude of wetland CH$_4$ emissions (higher values of δ^{13}C and lower magnitude of CH$_4$) or smaller magnitude of OH sink (higher values of δ^{13}C). However, increasing wetland CH$_4$ emissions in summer would cause larger discrepancies in CH$_4$ abundance in summer-autumn (Warwick et al., 2016), and therefore, the magnitude of wetland CH$_4$ emissions are probably not only the cause for the observed discrepancies between model and observations. In addition, higher OH concentrations during

430 spring and early summer, and lower OH concentrations in autumn could lead to a better match with the observations. Note that changes in the emissions affect the modelled CH$_4$ and δ^{13}C with some lag (see Section 3.1.2), but changes in OH would lead to an instantaneous effect.

At NWR (Fig. 4) the $\Delta\delta^{13}$C observations increase gradually from the beginning of the year until summer (approx. DOY $\leq$ 200), and decreases until early winter (approx. DOY $\leq$ 300). The amplitude of the observed $\Delta\delta^{13}$C is 0.3 ‰, with $\sigma = 0.078$ ‰,

435 and the modelled amplitudes (0.12–0.13 ‰) are again less than half of the observations. All three simulations show depletion in summer, ~50 days later than observations suggest. The depletion in summer and autumn is not as strong as in ALT, and the models follow the depletion better than in ALT, although the minima are slightly shallower compared to the observations. Compared to ALT, the summer enrichment of $\Delta\delta^{13}$C is relatively stronger at NWR. The observations show strong enrichment at around DOY = 200, but none of the simulation could reproduce the peak. The discrepancies are high, especially in the

440 simulations using EDGAR v4.3.2. In SIM_E432_EFMMNS the modelled $\Delta\delta^{13}$C stays constant until around DOY = 125, while the modelled $\Delta\delta^{13}$C first increases in SIM_E5. SIM_E432 again shows a strong depletion between DOY 50–100, as in ALT. Nevertheless, all the simulations reach a similar maximum at around DOY = 225.

The amplitude of the modelled ΔCH$_4$ is about 7 % smaller in SIM_E5 (31.5 ppb) and 18–31 % larger in SIM_E432 (44.0 ppb) and in SIM_E432_EFMMNS (39.8 ppb) compared to the observations (33.7 ppb). The modelled ΔCH$_4$ follow

445 the observations well until DOY = 75 in SIM_E432_EFMMNS. The observations reach at maximum at around DOY = 75. After DOY = 75 that, modelled CH$_4$ in SIM_E432 and SIM_E432_EFMMNS continues to increase until approx. DOY = 125, while SIM_E5 remains more or less constant until DOY=125, following the observations well. The timing of the minimum, however, does not differ much: the observations reach a minimum value at approx. DOY = 200, while all the simulations reach its minima at about DOY = 225. All the simulations show slight underestimation of ΔCH$_4$ in winter. The differences

450 between modelled and observed $\Delta\delta^{13}$C in SIM_E5 therefore could be due to wrong proportion of biogenic (heavily depleted)

Atmospheric
Chemistry
and Physics
Discussions
Open Access
EGU

to fossil based (less depleted) emissions source especially during summer. The differences in SIM_E432 in spring suggest that the biogenic EFMM emissions are probably overestimated. However, although the seasonal cycle of EFMM emissions is removed, the spring discrepancies remain (SIM_E432_EFMMNS). In addition, the differences in both ΔCH_4 and $\Delta \delta^{13}C$ in winter suggest underestimation of biogenic emissions from all simulations.

3.3 Zonal means in the stratosphere

In this section, we examine the seasonal cycle in the zonal mean of $\Delta \delta^{13}C$ in the stratosphere, similarly to Section 3.1.1, averaged over the eight top most layers of TM5 (corresponds to levels with pressure between approx. 88–0 hPa). The stratospheric chemistry and transport are important such that those also affect the seasonal cycle in the troposphere to some extent. Note however, $\delta^{13}C$ observations in the upper atmosphere is limited to validate the modelled seasonal cycles, so this is simply a summary of the model results. Nevertheless, the model is able to simulate realistic ΔCH_4 and $\delta^{13}C$ profiles for the stratosphere compared to e.g. Röckmann et al. (2011) (Fig. not shown).

In the spin-up simulations, we could see that the seasonal cycle of $\delta^{13}C$ in the tropical stratosphere is influenced by the transport of air from the troposphere. The timescale for reaching a stable $\delta^{13}C$ seasonal cycle was therefore similar to that in the troposphere, i.e. ca. 2 years (Supplementary Fig. S5). Therefore, we consider the detrended seasonal cycle from 2002–2012 for the analysis. The temperature inversion in the stable stratified stratospheric air leads to slow vertical transport, with transport timescales of a few years. The slow transport caused the seasonal cycle of $\delta^{13}C$ to stabilize in less time in mid and high latitudes than in the tropics (Figure not shown) in the spin-up simulations. Therefore, the timescale for chemistry is shorter than for transport, and the $\delta^{13}C$ is less influenced by the tropospheric air masses and the $\delta^{13}C$ corresponds to the KIE of the stratospheric sinks.

The photochemical sinks in the stratosphere together with the Brewer-Dobson circulation causes the amplitudes in the seasonal cycle of both ΔCH_4 and $\Delta \delta^{13}C$ to become much larger in the stratosphere (47–103 ppb, and 0.53–1.28 ‰) than in the troposphere. The shape of the $\Delta \delta^{13}C$ seasonal cycles is again generally mirroring the cycle of ΔCH_4. This is expected, as the KIE of all sinks (OH, Cl and O(^{1}D)) in the stratosphere is larger than 1.

The phase shifts are less clear in the stratosphere (correlation $p_0 \leq 0.96$ and $R^2 \geq 0.92$), indicating that the effect of emissions on $\Delta \delta^{13}$ seasonality is small (Supplementary Fig. S6). This is in line with the conclusion from the spin-up simulations described above. This also results in negligible differences in Deltaδ^{13} seasonality between the simulations that differ in their surface emissions (figure not shown).

The phase ellipse at 60° S–90° S yet does not form a straight line, such that the increase in $\Delta \delta^{13}C$ in the beginning of the year is relatively slower than the decrease in ΔCH_4 compared to the second half of the year (Supplementary Fig. S6). This is probably due to seasonal effect of the transport as well as seasonal changes in the species that contribute to the sink. At high latitudes, the Brewer-Dobson circulation affects the methane distribution strongly, leading to a decrease in CH_4 towards winter with $^{13}CH_4$ enriched air masses. Because the Brewer-Dobson circulation is stronger in the Southern Hemisphere, the effect is especially prominent in the southern high latitudes (60° S–90° S) (Fig. 5 and Supplementary Fig. S6). The maxima in the tropical region (30° S–EQ and EQ–30° N) follow the position of the strongest vertical motion, i.e. influx of methane rich air
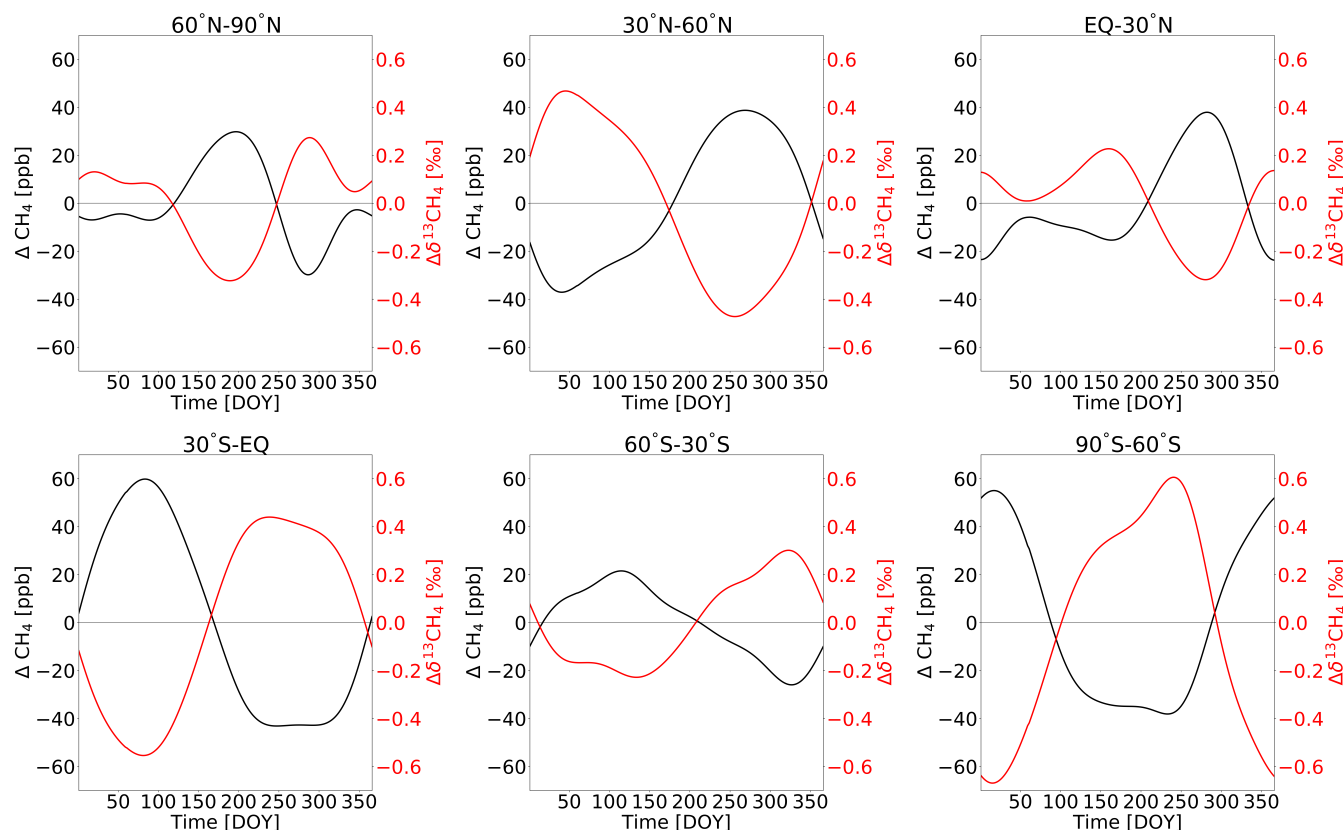
Figure 5. Seasonal cycle in zonal mean ΔCH_4 and $\Delta\delta^{13}C$. The data is averaged over the eight uppermost model layers. The daily averages are calculated from 2002–2012 based on SIM_E5.

485   from the troposphere. The asymmetry in the amplitude in the tropical seasonal cycles show the difference in the strength of the vertical motion.

4 Discussion

4.1 Isotope signatures

The seasonality of $\delta^{13}C$ depends on by the isotopic signature of the emissions. Ganesan et al. (2018) showed that changing the

490   source signatures by about ±13 ‰ affects the modelled $\delta^{13}C$ more than ± 0.5 ‰. Furthermore, our spin-up tests also indicate that changing the isotopic signature by ± 1 ‰ can reduce/increase the $\delta^{13}C$ seasonal cycle amplitude by 1.5–7 times, and the timing of minima/maxima by 7–130 days at 30° latitudinal bands (Supplementary Fig. S7). Considering that our results agree well with the observations at the South Pole, we could assume that the currently used isotopic signatures are correct in a broad

sense, and that more detailed and a better spatial and temporal distribution of the signature values would improve the agreement

495 with observations.

Although we have used a recently published spatial distributions of source signatures where available, there are still large uncertainties in the modelled δ^{13}C values due to e.g. the vegetation types, especially tropical wetlands (Ganesan et al., 2018). Tropical wetlands are more enriched with C-13 compared to high-latitude wetlands partly because warmer wetlands have often a thicker oxic layer, and in part because of differences in methanogenic communities, and in part because of different plant

500 material; high-latitude wetlands precursor plant material is C3, which is depleted in C-13, while in the Tropics the dominant plant material is C4 (Fisher et al., 2011).

The coal source signatures vary depending on coal types, depths, coalification processes, type of mining and coal rank (Zazzeri et al., 2016), but only limited measurements and country-level data for coal mining types are available, and may be misreported (Feinberg et al., 2018) as the coal source signature can also vary within in a country (Zazzeri et al., 2016).

505 EFMM source signatures are dependent on types of feed (Feinberg et al., 2018; Chang et al., 2019; Levin et al., 1993), and therefore isotopic signature can be determined by the fraction of major vegetation types (Chang et al., 2019), i.e. C4 and C3 plants (Still et al., 2003). However, the vegetation distribution in a region may not correspond to the livestock diet. Ruminant C3 diet leads to more depleted values of δ^{13}C emissions (Brownlow et al., 2017). Manure management isotopic source signatures depend on manure type; liquid manure is more depleted in $^{13}CH_4$, than manure pile emissions (Levin et al., 1993).

510 Rice cultivation methods also affect the source signatures. Mulching cultivation leads to higher values of δ^{13}C compared to traditional cultivation, and to lower CH_4 total emissions (Zhang et al., 2017). In this study, we used a global uniform value of -62.1 ‰ for RICE emissions, but measured values vary between approximately -45 ‰ and -65 ‰ at three different rice fields in China (Zhang et al., 2017). The seasonality of δ^{13}C is determined by cultivation method, tillage and Nitrogen (N) fertilization, but is also controlled by drainage. For instance, permanently flooded rice fields have enriched δ^{13}C values at the beginning

515 of the crop season followed by a rapid depletion in $^{13}CH_4$ and towards end of the season δ^{13}C values become enriched again (Zhang et al., 2017). In double harvest fields, the $\delta^{13}CH_4$ values are depleted immediately after drainage (Zhang et al., 2017).

Biomass burning emissions have strong $^{13}CH_4$ seasonality due to burning activity and vegetation types, especially in African Savannah, (Brownlow et al., 2017). C4 plants in African Savannah are abundant, and during the burning period, usually between December and March, δ^{13}C is shifted towards less negative (Brownlow et al., 2017). Pine forest burns in southeastern USA are

520 more depleted with $^{13}CH_4$ (-21 ‰ to -29.5 ‰) compared to African grassland burning (-16.6 ‰ to -26.1 ‰), while African woodland burns produce methane with -30 ‰ (Chanton et al., 2000). The $\delta^{13}CH_4$ signature of biomass burning varies during different phases, i.e., the smouldering phase it produces more depleted methane compared to flaming phase (Chanton et al., 2000). However, the main factor determining δ^{13}C is plant type C3 or C4 (Quay et al., 1991).

In addition, we acknowledge that KIE of soil sinks varies among soil types. Snover and Quay (2000) measured 1.0173 and

525 1.0181 for temperate grasslands and forest in Washington Sate, USA, respectively. In addition, Tyler et al. (1994b) measured a value of 1.022 in College Woods in Durham, New Hampshire, USA. Reeburgh et al. (1997) measured values between 1.022–1.025 in boreal forest in Bonanza Creek, Alaska, USA. Those may also vary with temperature and CH_4 concentration due to variation of biological KIE (Tyler et al., 1994b).

Furthermore, source signatures may have seasonal variations. These variations have been reported for biogenic sources,
530 such as wetlands, rice cultivation and ruminants. Wetlands are expected to have temporal variations depending on emission
processes (Fisher et al., 2017). Forested bogs have larger temporal variations of δ^{13}C emissions compared to poor fen, and the
CH$_4$ emitted from fen is more enriched with C-13 compared to bog emissions (Kelly et al., 1992).

Rice cultivation source signatures also have temporal variations (Tyler et al., 1994a; Bergamaschi, 1997). The exact reasons
for the variations are unclear, but possible explanations include changes in the methanogensis pathway (Whiticar et al., 1986),
535 changes in the relative rates of production and oxidation of CH$_4$ with time (Kelly et al., 1992) and a temperature dependence
of the isotope effects in the production of methane (Blair et al., 1993).

As ruminant source signatures are dependent on feed type, the source signatures may have a seasonal cycle and annual
variations when the cattle diet changes (Lopez et al., 2017). Seasonal changes in manure management may be affected similarly,
but the exact values are yet not well quantified.

540 ## 4.2 Seasonal cycle of CH$_4$ emissions

The modelled δ^{13}C cycle is found to be mostly affected by wetland emissions, and therefore, δ^{13}C measurements could be used
to evaluate CH$_4$ emission magnitude and seasonal cycle of wetland emissions. Wetland CH$_4$ emissions at high latitudes (north
of 50° N) estimated by process-based models (Melton et al., 2013; Bloom et al., 2017) find a maximum in May-August, and
inverse models (Bousquet et al., 2011) find a maximum in July. Studies based on δ^{13}C measurements indicate that the high-
545 latitude CH$_4$ emissions likely peak in August. (Warwick et al., 2016; Fujita et al., 2018; Thompson et al., 2018). Thompson
et al. (2017) showed that the LPJ-DGVM vegetation model estimates CH$_4$ wetland emissions to peak between May and June,
depending on the region within the Northern High Latitudes (NHL; north of 50° N), which is considerably earlier than inversion
models (July–September). LPX-Bern v1.4 wetland emissions used in this study has maximum emissions at NHL occurring in
September, later than other studies. Aalto et al. (2021) showed that the main reasons for the late maximum in LPX-Bern v1.4 is
550 the strong precipitation dependence of wetland emissions. In addition, the maximum NHL CH$_4$ emission in LPX-Bern v1.4 is
approximately 3 Tg CH$_4$ month^{-1} lower than those in Fung et al. (1991), used in Warwick et al. (2016), and the Saunois et al.
(2020) bottom-up model ensemble mean. Tenkanen et al. (2021) also showed that emissions in the NHL are ~6 Tg CH$_4$/yr
greater than in LPX-Bern v1.4, based on an inversion using ground-based atmospheric CH$_4$ data. Top-down and bottom-up
estimates differ much in 60° N–90° N, with top-down estimates being 40–49 % of the bottom-up estimates (Saunois et al.,
555 2020). However, Warwick et al. (2016) showed that the emission magnitude should be approximately doubled to resolve the
δ^{13}C amplitude as observed in e.g. ALT. It may be unrealistic to assume that wetland emissions in high northern latitudes are
underestimated so significantly, but spatial distribution of the emissions (reference), the other natural biogenic emissions, such
as those from inland water systems (Rosentreter et al., 2021) and the effects of the upland soil sink on ^{13}C (Oh et al., 2020)
may well be reasons for the underestimation of the δ^{13}C amplitude at high latitudes in this study.

560 In the Amazon, the climatological monthly biogenic CH$_4$ flux based on column budgeting (difference of the CH$_4$ column
content is due to the sum of fluxes along the air parcel path) displays two peaks, one in February and another in September–
October (Basso et al., 2016). An inversion study over Brazil suggests wetland emissions peak in February and March (Tun-

nicliffe et al., 2020). Our 30° S–EQ averaged wetland emission also shows a high peak in February. However, the peak in

September–October is not present. However, results from SCHIAMACHY (Bloom et al., 2012) over the Amazon show that

565   in SH Tropics, the peak is likely to appear in December–February and near the equator the peak is in February–April and a

bit to the north in June-August. These differences in wetland emission timing between NH and SH Tropics correspond to the

LPX-Bern results used in this study. In addition, the ENSO phase also affects the inter-annual variability of wetland emissions

in tropical wetlands, enhancing tropical wetland emission during La Niña (Pandey et al., 2017; Zhu et al., 2017).

Other important emissions in the Tropics is from the fires. Fires in the Amazonian region occur in August-December, with

570   a peak in November (Basso et al., 2016), in line with the GFED emissions used in this study.

CH_4 emissions from rice follow the rice growing calendar (Cao et al., 1996). Cao et al. (1996) modelled CH_4 emission from

rice with a maximum in July–September north of 20° N, and in December–February in the south of 10° S, while near the

equatorial regions emissions are high throughout the year, peaking in August. Zhang et al. (2016) also estimated global rice

CH_4 emissions to peak in July–August. Measurements performed during the growing season (Bergamaschi, 1997; Tyler et al.,

575   1994a) agree with these estimates. CH_4 emissions from rice cultivation, provided by EDGAR v5.0 correspond better to these

estimates and numbers than emissions from EDGAR v4.3.2.

The seasonal cycle of CH_4 emissions from the EFMM sector also varies consideraby between the EDGAR versions. A study

based on dairy cows and ewes in New-Zealand showed that the seasonal changes follow the different amounts of feed intake

and seasonal variation in milk production for dairy cows compared to ewes (Ulyatt et al., 2002). The study found maximum

580   emissions in September, while the estimated minimum emissions vary between June and March, depending on whether feed

intake is taken into account. This is more in line with EDGAR v4.3.2 compared to v5.0 at 30° S–90° S. A study performed

in South Africa, concluded that Nguni and Boran cows produce more CH_4 per kilogram live weight of cow during the dry

season (mid-May to October) compared to the wet season (November to early May) (Mapfumo et al., 2018), which partly

corresponds to EFMM emissions peaking in August-October in EDGARv4.3.2 at 30° S–90° S. In contrast, Arndt et al. (2018)

585   measured emissions from Jersey cattle (primary breed) in California and found that animal housing (enteric fermentation as

major source) had no seasonality, which corresponds well to EDGAR v5.0. Chen et al. (2018) found only weak seasonality

for livestock emissions, but warmer air temperature is likely to enhance manure CH_4 emissions, contradicting both EDGAR

versions.

Manure management has a seasonal cycle depending on liquid manure storage empty-full level and the temperature of the

590   manure (VanderZaag et al., 2014). VanderZaag et al. (2014) measured whole farm emissions (EFMM) in Ontario, Canada to

be larger in autumn compared to spring, contrary to EDGAR v4.3.2 peak at 30° N–60° N, which is opposite. Cárdenas et al.

(2021) showed that the temperature at which manure is stored affects the amount of emitted CH_4, such that during summer

CH4 emission is greater, but when the temperature drops below 13.39 °C,CH_4 emissions from manure are low. Arndt et al.

(2018) also concluded that CH_4 emission measured in California, USA from liquid manure storage are larger during summer

595   than in the winter. Husted (1994) also found that CH_4 emission from slurries increases with storage temperatures. However,

these findings do not correspond to either EDGAR version at 30° N–60° N.

4.3 Atmospheric sinks

OH is the largest CH_4 sink in the atmosphere, and it removes $^{12}CH_4$ faster than $^{13}CH_4$. The seasonal cycle of OH is affected by humidity, clouds, temperature and forest fires, and Rohrer and Berresheim (2006) estimated that ~23 % of long-term variations in OH concentrations can be explained by seasonality. Lowe et al. (2004) speculated that their underestimation of the $\delta^{13}C$ seasonal cycle amplitude in the Tropics may be associated with the OH sink, while Allan et al. (2001b) suggested the overestimation of CH_4 seasonal cycle in the model is associated with an overestimate of OH sink by more than 28 %. We examined the $\delta^{13}C$ seasonal cycle by changing the seasonal cycle amplitude of the OH concentrations by ± 10 %, but the effect on the tropospheric $\delta^{13}C$ seasonal cycle with respect to CH_4 was insignificant even in the Tropics (figure not shown).

Marine boundary layer Cl is thought to have a non-negligible contribution in CH_4 sink, with estimates 5–25 Tg yr^{-1} in range (Allan et al., 2001b, 2007). Due to its stronger fractionation compared to that of OH, underestimation of tropospheric Cl will likely lead to underestimation of the $\delta^{13}C$ seasonal cycle amplitude in the troposphere, assuming that Cl concentration has similar seasonality as OH (Allan et al., 2007; Wang et al., 2019). In this study, we did not include the tropospheric Cl sink, but could nevertheless reproduce the CH_4 and $\delta^{13}C$ seasonal cycle measured at the South Pole reasonably well. As emission seasonality affects this site only marginally, the seasonality at the SPO is mostly driven by atmospheric sinks. Although it has been shown that marine BL Cl concentration is the highest in the Tropics (e.g. Hossaini et al., 2016), our results support the recent study by Gromov et al. (2018) who suggested that the contribution of the tropospheric Cl sink to atmospheric CH_4 budgets are small. Our model results show that the CH_4 to $\delta^{13}C$ ratio does not follow the theoretical KIE line at the southern high latitude, similarly to the observation based study by Allan et al. (2001b). They argued that the kinetic isotope fractionation at a site in the SH extratropics require an CH_4 oxidation pathway by Cl.

5 Summary and conclusions

We performed a global analysis of how different CH_4 emission sources influence the $\delta^{13}C$ seasonal cycle, averaged over 30° latitudinal bands during 2000–2012, using the TM5 atmospheric chemistry transport model. Based on the simulation results, wetland emissions are found to be the dominant CH_4 source driving the $\delta^{13}C$ seasonal cycle, apart from atmospheric sinks. Wetland emissions are the key, especially in determining the timing of $\delta^{13}C$ minimum peaks in the NH. Comparisons using EDGAR v5.0, v4.3.2, and additional emission scenarios removing the seasonal cycle of emissions from enteric fermentation and manure management (EFMM) in v4.3.2 show that EFMM emissions in v4.3.2 are responsible for the unique $\delta^{13}C$ depletion in the NH in spring.

Seasonal cycles in $\Delta\delta^{13}C$ are reverse of ΔCH_4 cycles in general, with a significant anti-correlation. However, due to the effects of the emissions, the phase ellipses do not form a straight line, but rather oval shapes, especially in the NH. At 30° S–EQ, the phase ellipse forms an irregular shape due to the effect of wetland and biomass burning emissions, which have distinct isotopic signatures and emission cycles. We also found that the effect of sinks other than OH contribute to the $\Delta\delta^{13}C$ cycle in relation to ΔCH_4 cycle. The phase ellipse did not become a straight line in 60° N–90° N even when seasonality of the

emissions is removed, suggesting the effect of soil sink, and the KIE-line slope in the deep SH (90° S–60° S) did not exactly

630   follow those when only the OH sink is considered.

Compared to INSTAAR observations at the South Pole station, Antarctica, the model is able to reproduce the $\Delta\delta^{13}$C seasonal cycle well, indicating that seasonality of the sinks and to a lesser extend in the emissions in the model are at the right level. For δ^{13}C observations closer to the emission sources, at Alert, Canada and Niwot Ridge, USA, the moel estimates using EDGAR v5.0 are in closer agreement to the observations than those using v4.3.2. The seasonal cycle of EFMM causes a δ^{13}C depletion

635   in spring in Alert and Niwot Ridge, which is not in the observations, suggesting that the seasonal cycle of EFMM is not correct in EDGAR v4.3.2. In addition, the modelled $\Delta\delta^{13}$C seasonal cycle amplitude is underestimated and maximum and minimum for $\Delta\delta^{13}$C are around 20 days later than the observations in Alert. The cause of these discrepancies may be underestimation of wetland CH_4 emissions in the northern high latitudes in summer, although some other factors, e.g. timing of wetland emission peak, seasonal cycle of OH, and isotopic signatures could also affect the simulated seasonal cycles.

640   Seasonal cycle amplitudes of both $\Delta\delta^{13}$C and ΔCH_4 are much larger in the stratosphere than in the troposphere. The effect of emissions is negligible in the stratosphere, and the δ^{13}C seasonality is therefore driven by the atmospheric sinks. However, due to lack of δ^{13}C observations at high altitudes, it is difficult to evaluate whether our estimated seasonal cycles are realistic.

Here, we have focused on the effects of emissions and their source signatures on the simulated seasonal cycle of δ^{13}C. There is an increasing number of studies examining the spatial and temporal distributions of emission signatures, but further research

645   at regional to global scales is needed to examine global changes of δ^{13}C. Furthermore, a step forward to better understand the different source contributions would be to build an atmospheric inversion, and will be the scope of our next study.

Author contributions.   VK, AT and TA designed the experiments. VK and AT developed the model code with help from LB, SH, AS and

650   MK. VK and AT performed the simulations. VK, AT, LB, PM and TA performed the analysis. ED, SM and JW provided the observational data. VK prepared the manuscript with contributions from all co-authors.

Atmospheric
Chemistry
and Physics
Discussions

References

660   Aalto, T., Tsuruta, A., Mäkelä, J., Mueller, J., Tenkanen, M., Burke, E., Chadburn, S., Gao, Y., Kangasaho, V., Kleinen, T., Lee, H., Leppänen, A., Markkanen, T., Materia, S., Miller, P., Peano, D., Peltola, O., Raivonen, M., Saunois, M., Wårlind, D., and Zaehle, S.: Air temperature and precipitation constraining the modelled wetland methane emissions in a boreal region in Northern Europe, Biogeosciences, to be submitted, 2021.

Allan, W., Lowe, D. C., and Cainey, J. M.: Active chlorine in the remote marine boundary layer: Modeling anomalous measurements
665   of $\delta13C$ in methane, Geophysical Research Letters, 28, 3239–3242, https://doi.org/https://doi.org/10.1029/2001GL013064, _eprint: https://onlinelibrary.wiley.com/doi/pdf/10.1029/2001GL013064, 2001a.

Allan, W., Manning, M. R., Lassey, K. R., Lowe, D. C., and Gomez, A. J.: Modeling the variation of $\delta13C$ in atmospheric methane: Phase ellipses and the kinetic isotope effect, Global Biogeochemical Cycles, 15, 467–481, https://doi.org/https://doi.org/10.1029/2000GB001282, _eprint: https://onlinelibrary.wiley.com/doi/pdf/10.1029/2000GB001282, 2001b.

670   Allan, W., Struthers, H., and Lowe, D. C.: Methane carbon isotope effects caused by atomic chlorine in the marine boundary layer: Global model results compared with Southern Hemisphere measurements, Journal of Geophysical Research: Atmospheres, 112, https://doi.org/10.1029/2006JD007369, _eprint: https://agupubs.onlinelibrary.wiley.com/doi/pdf/10.1029/2006JD007369, 2007.

Arndt, C., Leytem, A., Hristov, A., Zavala-Araiza, D., Cativiela, J., Conley, S., Daube, C., Faloona, I., and Herndon, S.: Short-term methane emissions from 2 dairy farms in California estimated by different measurement techniques and US Environmental Protection Agency
675   inventory methodology: A case study, Journal of Dairy Science, 101, 11 461–11 479, https://doi.org/10.3168/jds.2017-13881, 2018.

Basso, L. S., Gatti, L. V., Gloor, M., Miller, J. B., Domingues, L. G., Correia, C. S. C., and Borges, V. F.: Seasonality and interannual variability of CH4 fluxes from the eastern Amazon Basin inferred from atmospheric mole fraction profiles, Journal of Geophysical Research: Atmospheres, 121, 168–184, https://doi.org/10.1002/2015JD023874, _eprint: https://onlinelibrary.wiley.com/doi/pdf/10.1002/2015JD023874, 2016.

680   Bergamaschi, P.: Seasonal variations of stable hydrogen and carbon isotope ratios in methane from a Chinese rice paddy, Journal of Geophysical Research: Atmospheres, 102, 25 383–25 393, https://doi.org/https://doi.org/10.1029/97JD01664, _eprint: https://onlinelibrary.wiley.com/doi/pdf/10.1029/97JD01664, 1997.

Bergamaschi, P., Brühl, C., Brenninkmeijer, C. a. M., Saueressig, G., Crowley, J. N., Grooß, J. U., Fischer, H., and Crutzen, P. J.: Implications of the large carbon kinetic isotope effect in the reaction CH4 + Cl for the 13C/12C ratio of stratospheric CH4, Geophysical Research
685   Letters, 23, 2227–2230, https://doi.org/10.1029/96GL02139, 1996.

Bergamaschi, P., Bräunlich, M., Marik, T., and Brenninkmeijer, C. A. M.: Measurements of the carbon and hydrogen isotopes of atmospheric methane at Izaña, Tenerife: Seasonal cycles and synoptic-scale variations, Journal of Geophysical Research: Atmospheres, 105, 14 531–14 546, https://doi.org/https://doi.org/10.1029/1999JD901176, _eprint: https://agupubs.onlinelibrary.wiley.com/doi/pdf/10.1029/1999JD901176, 2000.

690   Bergamaschi, P., Karstens, U., Manning, A. J., Saunois, M., Tsuruta, A., Berchet, A., Vermeulen, A. T., Arnold, T., Janssens-Maenhout, G., Hammer, S., Levin, I., Schmidt, M., Ramonet, M., Lopez, M., Lavric, J., Aalto, T., Chen, H., Feist, D. G., Gerbig, C., Haszpra, L., Hermansen, O., Manca, G., Moncrieff, J., Meinhardt, F., Necki, J., Galkowski, M., O'Doherty, S., Paramonova, N., Scheeren, H. A., Steinbacher, M., and Dlugokencky, E.: Inverse modelling of European CH4 emissions during 2006–2012 using different inverse models and reassessed atmospheric observations, Atmospheric Chemistry and Physics, 18, 901–920, https://doi.org/https://doi.org/10.5194/acp-
695   18-901-2018, 2018.

Blair, N. E., Boehme, S. E., and Carter, W. D.: The Carbon Isotope Biogeochemistry of Methane Production in Anoxic Sediments: 1.
Field Observations, in: Biogeochemistry of Global Change: Radiatively Active Trace Gases Selected Papers from the Tenth International
Symposium on Environmental Biogeochemistry, San Francisco, August 19–24, 1991, edited by Oremland, R. S., pp. 574–593, Springer
US, Boston, MA, https://doi.org/10.1007/978-1-4615-2812-8_31, 1993.

700 Bloom, A. A., Palmer, P. I., Fraser, A., and Reay, D. S.: Seasonal variability of tropical wetland CH$_4$ emissions: the role of the methanogen-
available carbon pool, Biogeosciences, 9, 2821–2830, https://doi.org/https://doi.org/10.5194/bg-9-2821-2012, 2012.

Bloom, A. A., Bowman, K. W., Lee, M., Turner, A. J., Schroeder, R., Worden, J. R., Weidner, R., McDonald, K. C., and Jacob, D. J.: A global
wetland methane emissions and uncertainty dataset for atmospheric chemical transport models (WetCHARTs version 1.0), Geoscientific
Model Development, 10, 2141–2156, https://doi.org/https://doi.org/10.5194/gmd-10-2141-2017, 2017.

705 Bousquet, P., Ringeval, B., Pison, I., Dlugokencky, E. J., Brunke, E.-G., Carouge, C., Chevallier, F., Fortems-Cheiney, A., Frankenberg,
C., Hauglustaine, D. A., Krummel, P. B., Langenfelds, R. L., Ramonet, M., Schmidt, M., Steele, L. P., Szopa, S., Yver, C., Viovy,
N., and Ciais, P.: Source attribution of the changes in atmospheric methane for 2006–2008, Atmos. Chem. Phys., 11, 3689–3700,
https://doi.org/10.5194/acp-11-3689-2011, 2011.

Brownlow, R., Lowry, D., Fisher, R. E., France, J. L., Lanoisellé, M., White, B., Wooster, M. J., Zhang, T., and Nisbet, E. G.: Isotopic Ratios
710 of Tropical Methane Emissions by Atmospheric Measurement: Tropical Methane δ ^{13} C Source Signatures, Global Biogeochemical
Cycles, 31, 1408–1419, https://doi.org/10.1002/2017GB005689, 2017.

Cantrell, C. A., Shetter, R. E., McDaniel, A. H., Calvert, J. G., Davidson, J. A., Lowe, D. C., Tyler, S. C., Cicerone, R. J., and Greenberg, J. P.:
Carbon kinetic isotope effect in the oxidation of methane by the hydroxyl radical, Journal of Geophysical Research: Atmospheres, 95,
22 455–22 462, https://doi.org/10.1029/JD095iD13p22455, _eprint: https://onlinelibrary.wiley.com/doi/pdf/10.1029/JD095iD13p22455,
715 1990.

Cao, M., Gregson, K., Marshall, S., Dent, J. B., and Heal, O. W.: Global Methane Emissions from Rice Paddies, Chemosphere, 33, 879–897,
https://doi.org/10.1016/0045-6535(96)00231-7, 1996.

Chang, J., Peng, S., Ciais, P., Saunois, M., Dangal, S. R. S., Herrero, M., Havlík, P., Tian, H., and Bousquet, P.: Revisiting en-
teric methane emissions from domestic ruminants and their δ 13 C CH4 source signature, Nature Communications, 10, 3420,
720 https://doi.org/10.1038/s41467-019-11066-3, number: 1 Publisher: Nature Publishing Group, 2019.

Chanton, J. P., Rutkowski, C. M., Schwartz, C. C., Ward, D. E., and Boring, L.: Factors influencing the stable carbon isotopic
signature of methane from combustion and biomass burning, Journal of Geophysical Research: Atmospheres, 105, 1867–1877,
https://doi.org/10.1029/1999JD900909, _eprint: https://agupubs.onlinelibrary.wiley.com/doi/pdf/10.1029/1999JD900909, 2000.

Chen, Z., Griffis, T. J., Baker, J. M., Millet, D. B., Wood, J. D., Dlugokencky, E. J., Andrews, A. E., Sweeney, C., Hu, C., and Kolka, R. K.:
725 Source Partitioning of Methane Emissions and its Seasonality in the U.S. Midwest, Journal of Geophysical Research: Biogeosciences,
123, 646–659, https://doi.org/10.1002/2017JG004356, _eprint: https://onlinelibrary.wiley.com/doi/pdf/10.1002/2017JG004356, 2018.

Crippa, M., Solazzo, E., Huang, G., Guizzardi, D., Koffi, E., Muntean, M., Schieberle, C., Friedrich, R., and Janssens-Maenhout,
G.: High resolution temporal profiles in the Emissions Database for Global Atmospheric Research, Scientific Data, 7, 121,
https://doi.org/10.1038/s41597-020-0462-2, number: 1 Publisher: Nature Publishing Group, 2020.

730 Crowley, J. N., Saueressig, G., Bergamaschi, P., Fischer, H., and Harris, G. W.: Carbon kinetic isotope effect in the reaction CH4+Cl: a
relative rate study using FTIR spectroscopy, Chemical Physics Letters, 303, 268–274, https://doi.org/10.1016/S0009-2614(99)00243-2,
1999.

Cárdenas, A., Ammon, C., Schumacher, B., Stinner, W., Herrmann, C., Schneider, M., Weinrich, S., Fischer, P., Amon, T., and Amon, B.: Methane emissions from the storage of liquid dairy manure: Influences of season, temperature and storage duration, Waste Management

735   (New York, N.Y.), 121, 393–402, https://doi.org/10.1016/j.wasman.2020.12.026, 2021.

de Laeter, J. R., Böhlke, J. K., Bièvre, P. D., Hidaka, H., Peiser, H. S., Rosman, K. J. R., and Taylor, P. D. P.: Atomic weights of the elements. Review 2000 (IUPAC Technical Report), 75, 683–800, https://doi.org/10.1351/pac200375060683, publisher: De Gruyter Section: Pure and Applied Chemistry, 2003.

Dee, D. P., Uppala, S. M., Simmons, A. J., Berrisford, P., Poli, P., Kobayashi, S., Andrae, U., Balmaseda, M. A., Balsamo, G., Bauer,

740   P., Bechtold, P., Beljaars, A. C. M., van de Berg, L., Bidlot, J., Bormann, N., Delsol, C., Dragani, R., Fuentes, M., Geer, A. J., Haimberger, L., Healy, S. B., Hersbach, H., Hólm, E. V., Isaksen, L., Kållberg, P., Köhler, M., Matricardi, M., McNally, A. P., Monge-Sanz, B. M., Morcrette, J.-J., Park, B.-K., Peubey, C., de Rosnay, P., Tavolato, C., Thépaut, J.-N., and Vitart, F.: The ERA-Interim reanalysis: configuration and performance of the data assimilation system, Quarterly Journal of the Royal Meteorological Society, 137, 553–597, https://doi.org/10.1002/qj.828, _eprint: https://rmets.onlinelibrary.wiley.com/doi/pdf/10.1002/qj.828, 2011.

745   Delwiche, K. B., Knox, S. H., Malhotra, A., Fluet-Chouinard, E., McNicol, G., Feron, S., Ouyang, Z., Papale, D., Trotta, C., Canfora, E., Cheah, Y.-W., Christianson, D., Alberto, M. C. R., Alekseychik, P., Aurela, M., Baldocchi, D., Bansal, S., Billesbach, D. P., Bohrer, G., Bracho, R., Buchmann, N., Campbell, D. I., Celis, G., Chen, J., Chen, W., Chu, H., Dalmagro, H. J., Dengel, S., Desai, A. R., Detto, M., Dolman, H., Eichelmann, E., Euskirchen, E., Famulari, D., Friborg, T., Fuchs, K., Goeckede, M., Gogo, S., Gondwe, M. J., Goodrich, J. P., Gottschalk, P., Graham, S. L., Heimann, M., Helbig, M., Helfter, C., Hemes, K. S., Hirano, T., Hollinger, D., Hörtnagl, L., Iwata,

750   H., Jacotot, A., Jansen, J., Jurasinski, G., Kang, M., Kasak, K., King, J., Klatt, J., Koebsch, F., Krauss, K. W., Lai, D. Y. F., Mammarella, I., Manca, G., Marchesini, L. B., Matthes, J. H., Maximon, T., Merbold, L., Mitra, B., Morin, T. H., Nemitz, E., Nilsson, M. B., Niu, S., Oechel, W. C., Oikawa, P. Y., Ono, K., Peichl, M., Peltola, O., Reba, M. L., Richardson, A. D., Riley, W., Runkle, B. R. K., Ryu, Y., Sachs, T., Sakabe, A., Sanchez, C. R., Schuur, E. A., Schäfer, K. V. R., Sonnentag, O., Sparks, J. P., Stuart-Haëntjens, E., Sturtevant, C., Sullivan, R. C., Szutu, D. J., Thom, J. E., Torn, M. S., Tuittila, E.-S., Turner, J., Ueyama, M., Valach, A. C., Vargas, R., Varlagin, A., Vazquez-Lule,

755   A., Verfaillie, J. G., Vesala, T., Vourlitis, G. L., Ward, E. J., Wille, C., Wohlfahrt, G., Wong, G. X., Zhang, Z., Zona, D., Windham-Myers, L., Poulter, B., and Jackson, R. B.: FLUXNET-CH4: A global, multi-ecosystem dataset and analysis of methane seasonality from freshwater wetlands, Earth System Science Data Discussions, pp. 1–111, https://doi.org/https://doi.org/10.5194/essd-2020-307, publisher: Copernicus GmbH, 2021.

Dlugokencky, E., Masarie, K., Tans, P., Conway, T., and Xiong, X.: Is the amplitude of the methane seasonal cycle changing?, Atmospheric

760   Environment, 31, 21–26, https://doi.org/10.1016/S1352-2310(96)00174-4, 1997.

Elsgaard, L., Olsen, A. B., and Petersen, S. O.: Temperature response of methane production in liquid manures and co-digestates, Science of The Total Environment, 539, 78–84, https://doi.org/10.1016/j.scitotenv.2015.07.145, 2016.

Etiope, G., Ciotoli, G., Schwietzke, S., and Schoell, M.: Gridded maps of geological methane emissions and their isotopic signature, Earth System Science Data, 11, 1–22, https://doi.org/https://doi.org/10.5194/essd-11-1-2019, 2019.

765   Feinberg, A. I., Coulon, A., Stenke, A., Schwietzke, S., and Peter, T.: Isotopic source signatures: Impact of regional variability on the δ13CH4 trend and spatial distribution, Atmospheric Environment, 174, 99 – 111, https://doi.org/https://doi.org/10.1016/j.atmosenv.2017.11.037, 2018.

Fisher, R. E., Sriskantharajah, S., Lowry, D., Lanoisellé, M., Fowler, C. M. R., James, R. H., Hermansen, O., Lund Myhre, C., Stohl, A., Greinert, J., Nisbet-Jones, P. B. R., Mienert, J., and Nisbet, E. G.: Arctic methane sources: Isotopic evidence for atmospheric inputs:

770   ARCTIC METHANE SOURCES, Geophysical Research Letters, 38, n/a–n/a, https://doi.org/10.1029/2011GL049319, 2011.

Fisher, R. E., France, J. L., Lowry, D., Lanoisellé, M., Brownlow, R., Pyle, J. A., Cain, M., Warwick, N., Skiba, U. M., Drewer, J., Dinsmore, K. J., Leeson, S. R., Bauguitte, S. J.-B., Wellpott, A., O'Shea, S. J., Allen, G., Gallagher, M. W., Pitt, J., Percival, C. J., Bower, K., George, C., Hayman, G. D., Aalto, T., Lohila, A., Aurela, M., Laurila, T., Crill, P. M., McCalley, C. K., and Nisbet, E. G.: Measurement of the 13C isotopic signature of methane emissions from north-
775   ern European wetlands, Global Biogeochemical Cycles, 31, 605–623, https://doi.org/https://doi.org/10.1002/2016GB005504, _eprint: https://agupubs.onlinelibrary.wiley.com/doi/pdf/10.1002/2016GB005504, 2017.

Fujita, R., Morimoto, S., Umezawa, T., Ishijima, K., Patra, P. K., Worthy, D. E. J., Goto, D., Aoki, S., and Nakazawa, T.: Temporal Variations of the Mole Fraction, Carbon, and Hydrogen Isotope Ratios of Atmospheric Methane in the Hudson Bay Lowlands, Canada, Journal of Geophysical Research: Atmospheres, 123, 4695–4711, https://doi.org/10.1002/2017JD027972, 2018.

780   Fung, I., John, J., Lerner, J., Matthews, E., Prather, M., Steele, L. P., and Fraser, P. J.: Three-dimensional model synthesis of the global methane cycle, Journal of Geophysical Research: Atmospheres, 96, 13 033–13 065, https://doi.org/https://doi.org/10.1029/91JD01247, _eprint: https://onlinelibrary.wiley.com/doi/pdf/10.1029/91JD01247, 1991.

Ganesan, A. L., Stell, A. C., Gedney, N., Comyn-Platt, E., Hayman, G., Rigby, M., Poulter, B., and Hornibrook, E. R. C.: Spatially Resolved Isotopic Source Signatures of Wetland Methane Emissions, Geophysical Research Letters, 45, 3737–3745,
785   https://doi.org/10.1002/2018GL077536, 2018.

Giglio, L., Randerson, J. T., and van der Werf, G. R.: Analysis of daily, monthly, and annual burned area using the fourth-generation global fire emissions database (GFED4), J. Geophys. Res. Biogeosci., 118, 317–328, https://doi.org/10.1002/jgrg.20042, 2013.

Gregory, D., Morcrette, J.-J., Jakob, C., Beljaars, A. C. M., and Stockdale, T.: Revision of convection, radiation and cloud schemes in the ECMWF integrated forecasting system, Q.J.R. Meteorol. Soc., 126, 1685–1710, https://doi.org/10.1002/qj.49712656607, 2000.

790   Gromov, S., Brenninkmeijer, C. A. M., and Jöckel, P.: A very limited role of tropospheric chlorine as a sink of the greenhouse gas methane, Atmospheric Chemistry and Physics, 18, 9831–9843, https://doi.org/10.5194/acp-18-9831-2018, publisher: Copernicus GmbH, 2018.

Hartmann, D., Klein Tank, A., Rusticucci, M., Alexander, L., Brönnimann, S., Charabi, Y., Dentener, F., Dlugokencky, E., Easterling, D., Kaplan, A., Soden, B., Thorne, P., Wild, M., and Zhai, P.: Observations: Atmosphere and Surface, book section 2, p. 159–254, Cambridge University Press, Cambridge, United Kingdom and New York, NY, USA, https://doi.org/10.1017/CBO9781107415324.008, 2013.

795   Hein, R., Crutzen, P. J., and Heimann, M.: An inverse modeling approach to investigate the global atmospheric methane cycle, Global Biogeochemical Cycles, 11, 43–76, https://doi.org/10.1029/96GB03043, 1997.

Hmiel, B., Petrenko, V. V., Dyonisius, M. N., Buizert, C., Smith, A. M., Place, P. F., Harth, C., Beaudette, R., Hua, Q., Yang, B., Vimont, I., Michel, S. E., Severinghaus, J. P., Etheridge, D., Bromley, T., Schmitt, J., Faïn, X., Weiss, R. F., and Dlugokencky, E.: Preindustrial 14 CH 4 indicates greater anthropogenic fossil CH 4 emissions, Nature, 578, 409–412, https://doi.org/10.1038/s41586-020-1991-8, number:
800   7795 Publisher: Nature Publishing Group, 2020.

Hossaini, R., Chipperfield, M. P., Saiz-Lopez, A., Fernandez, R., Monks, S., Feng, W., Brauer, P., and Glasow, R. v.: A global model of tropospheric chlorine chemistry: Organic versus inorganic sources and impact on methane oxi-dation, Journal of Geophysical Research: Atmospheres, 121, 14,271–14,297, https://doi.org/10.1002/2016JD025756, _eprint: https://onlinelibrary.wiley.com/doi/pdf/10.1002/2016JD025756, 2016.

805   Houweling, S., Krol, M., Bergamaschi, P., Frankenberg, C., Dlugokencky, E. J., Morino, I., Notholt, J., Sherlock, V., Wunch, D., Beck, V., Gerbig, C., Chen, H., Kort, E. A., Röckmann, T., and Aben, I.: A multi-year methane inversion using SCIAMACHY, accounting for systematic errors using TCCON measurements, Atmos. Chem. Phys., 14, 3991–4012, https://doi.org/10.5194/acp-14-3991-2014, 2014.

Huijnen, V., Williams, J., van Weele, M., van Noije, T., Krol, M., Dentener, F., Segers, A., Houweling, S., Peters, W., de Laat, J., Boersma, F., Bergamaschi, P., van Velthoven, P., Le Sager, P., Eskes, H., Alkemade, F., Scheele, R., Nédélec, P., and Pätz, H.-W.: The global

810   chemistry transport model TM5: description and evaluation of the tropospheric chemistry version 3.0, Geoscientific Model Development, 3, 445–473, https://doi.org/10.5194/gmd-3-445-2010, publisher: Copernicus GmbH, 2010.

Husted, S.: Seasonal Variation in Methane Emission from Stored Slurry and Solid Manures, Journal of Environmental Quality, 23, 585–592, https://doi.org/10.2134/jeq1994.00472425002300030026x, _eprint: https://onlinelibrary.wiley.com/doi/pdf/10.2134/jeq1994.00472425002300030026x, 1994.

815   Ito, A. and Inatomi, M.: Use of a process-based model for assessing the methane budgets of global terrestrial ecosystems and evaluation of uncertainty, Biogeosciences, 9, 759–773, https://doi.org/10.5194/bg-9-759-2012, 2012.

Janssens-Maenhout, G., Crippa, M., Guizzardi, D., Muntean, M., Schaaf, E., Dentener, F., Bergamaschi, P., Pagliari, V., Olivier, J. G. J., Peters, J. A. H. W., van Aardenne, J. A., Monni, S., Doering, U., Petrescu, A. M. R., Solazzo, E., and Oreggioni, G. D.: EDGAR v4.3.2 Global Atlas of the three major greenhouse gas emissions for the period 1970–2012, Earth System Science Data, 11, 959–1002,

820   https://doi.org/10.5194/essd-11-959-2019, 2019.

Javadinejad, S., Eslamian, S., and Ostad-Ali-Askari, K.: Investigation of monthly and seasonal changes of methane gas with respect to climate change using satellite data, Applied Water Science, 9, 180, https://doi.org/10.1007/s13201-019-1067-9, 2019.

Jöckel, P., Tost, H., Pozzer, A., Brühl, C., Buchholz, J., Ganzeveld, L., Hoor, P., Kerkweg, A., Lawrence, M. n., G, Sander, R., Steil, B., Stiller, G., Tanarhte, M., Taraborrelli, D., Aardenne, J. v., and Lelieveld, J.: The atmospheric chemistry general circulation model

825   ECHAM5/MESSy1: consistent simulation of ozone from the surface to the mesosphere, Atmospheric Chemistry and Physics, 6, 5067–5104, https://doi.org/https://doi.org/10.5194/acp-6-5067-2006, 2006.

Kelly, C. A., Dise, N. B., and Martens, C. S.: Temporal variations in the stable carbon isotopic composition of methane emitted from Minnesota peatlands, Global Biogeochemical Cycles, 6, 263–269, https://doi.org/https://doi.org/10.1029/92GB01478, _eprint: https://onlinelibrary.wiley.com/doi/pdf/10.1029/92GB01478, 1992.

830   Khalil, M. a. K. and Rasmussen, R. A.: Sources, sinks, and seasonal cycles of atmospheric methane, Journal of Geophysical Research: Oceans, 88, 5131–5144, https://doi.org/10.1029/JC088iC09p05131, _eprint: https://onlinelibrary.wiley.com/doi/pdf/10.1029/JC088iC09p05131, 1983.

Kivimäki, E., Lindqvist, H., Hakkarainen, J., Laine, M., Sussmann, R., Tsuruta, A., Detmers, R., Deutscher, N. M., Dlugokencky, E. J., Hase, F., Hasekamp, O., Kivi, R., Morino, I., Notholt, J., Pollard, D. F., Roehl, C., Schneider, M., Sha, M. K., Velazco, V. A., Warneke,

835   T., Wunch, D., Yoshida, Y., and Tamminen, J.: Evaluation and Analysis of the Seasonal Cycle and Variability of the Trend from GOSAT Methane Retrievals, Remote Sensing, 11, 882, https://doi.org/10.3390/rs11070882, number: 7 Publisher: Multidisciplinary Digital Publishing Institute, 2019.

Krol, M., Houweling, S., Bregman, B., Broek, M. v. d., Segers, A., Velthoven, P. v., Peters, W., Dentener, F., and Bergamaschi, P.: The two-way nested global chemistry-transport zoom model TM5: algorithm and applications, Atmospheric Chemistry and Physics, 5, 417–432,

840   https://doi.org/https://doi.org/10.5194/acp-5-417-2005, 2005.

Kuze, A., Kikuchi, N., Kataoka, F., Suto, H., Shiomi, K., and Kondo, Y.: Detection of Methane Emission from a Local Source Using GOSAT Target Observations, Remote Sensing, 12, 267, https://doi.org/10.3390/rs12020267, number: 2 Publisher: Multidisciplinary Digital Publishing Institute, 2020.

Lambert, G. and Schmidt, S.: Reevaluation of the oceanic flux of methane: Uncertainties and long term variations, Chemosphere, 26, 579 –

845   589, https://doi.org/https://doi.org/10.1016/0045-6535(93)90443-9, proceedings of the NATO advanced research workshop, 1993.

Lan, X., Basu, S., Schwietzke, S., Bruhwiler, L. M. P., Dlugokencky, E. J., Michel, S. E., Sherwood, O. A., Tans, P. P., Thoning, K., Etiope, G., Zhuang, Q., Liu, L., Oh, Y., Miller, J. B., Pétron, G., Vaughn, B. H., and Crippa, M.: Improved Constraints on Global Methane Emissions and Sinks Using δ13C-CH4, Global Biogeochemical Cycles, 35, e2021GB007 000, https://doi.org/10.1029/2021GB007000, _eprint: https://onlinelibrary.wiley.com/doi/pdf/10.1029/2021GB007000, 2021.

850   Levin, I., Bergamaschi, P., Dörr, H., and Trapp, D.: Stable isotopic signature of methane from major sources in Germany, Chemosphere, 26, 161–177, https://doi.org/10.1016/0045-6535(93)90419-6, 1993.

Lienert, S. and Joos, F.: A Bayesian ensemble data assimilation to constrain model parameters and land-use carbon emissions, Biogeosciences, 15, 2909–2930, https://doi.org/https://doi.org/10.5194/bg-15-2909-2018, publisher: Copernicus GmbH, 2018.

Lopez, M., Sherwood, O. A., Dlugokencky, E. J., Kessler, R., Giroux, L., and Worthy, D. E. J.: Isotopic signatures of anthropogenic CH4
855   sources in Alberta, Canada, Atmospheric Environment, 164, 280–288, https://doi.org/10.1016/j.atmosenv.2017.06.021, 2017.

Lowe, D. C., Koshy, K., Bromley, T., Allan, W., Struthers, H., Mani, F., and Maata, M.: Seasonal cycles of mixing ratio and 13C in atmospheric methane at Suva, Fiji, Journal of Geophysical Research: Atmospheres, 109, https://doi.org/https://doi.org/10.1029/2004JD005166, _eprint: https://agupubs.onlinelibrary.wiley.com/doi/pdf/10.1029/2004JD005166, 2004.

Mapfumo, L., Grobler, S. M., Mupangwa, J. F., Scholtz, M. M., and Muchenje, V.: Enteric methane output from selected herds of beef cattle
860   raised under extensive arid rangelands, Pastoralism, 8, 15, https://doi.org/10.1186/s13570-018-0121-9, 2018.

Melton, J. R., Wania, R., Hodson, E. L., Poulter, B., Ringeval, B., Spahni, R., Bohn, T., Avis, C. A., Beerling, D. J., Chen, G., Eliseev, A. V., Denisov, S. N., Hopcroft, P. O., Lettenmaier, D. P., Riley, W. J., Singarayer, J. S., Subin, Z. M., Tian, H., Zürcher, S., Brovkin, V., van Bodegom, P. M., Kleinen, T., Yu, Z. C., and Kaplan, J. O.: Present state of global wetland extent and wetland methane modelling: conclusions from a model inter-comparison project (WETCHIMP), Biogeosciences, 10, 753–788, https://doi.org/10.5194/bg-10-753-
865   2013, publisher: Copernicus GmbH, 2013.

Monteil, G., Houweling, S., Dlugockenky, E. J., Maenhout, G., Vaughn, B. H., White, J. W. C., and Rockmann, T.: Interpreting methane variations in the past two decades using measurements of CH$_4$ mixing ratio and isotopic composition, Atmospheric Chemistry and Physics, 11, 9141–9153, https://doi.org/10.5194/acp-11-9141-2011, 2011.

Nisbet, E. G., Dlugokencky, E. J., Manning, M. R., Lowry, D., Fisher, R. E., France, J. L., Michel, S. E., Miller, J. B., White, J. W. C.,
870   Vaughn, B., Bousquet, P., Pyle, J. A., Warwick, N. J., Cain, M., Brownlow, R., Zazzeri, G., Lanoisellé, M., Manning, A. C., Gloor, E., Worthy, D. E. J., Brunke, E.-G., Labuschagne, C., Wolff, E. W., and Ganesan, A. L.: Rising atmospheric methane: 2007–2014 growth and isotopic shift, Global Biogeochemical Cycles, 30, 1356–1370, https://doi.org/https://doi.org/10.1002/2016GB005406, 2016.

Nisbet, E. G., Manning, M. R., Dlugokencky, E. J., Fisher, R. E., Lowry, D., Michel, S. E., Myhre, C. L., Platt, S. M., Allen, G., Bousquet, P., Brownlow, R., Cain, M., France, J. L., Hermansen, O., Hossaini, R., Jones, A. E., Levin, I., Manning, A. C., Myhre, G., Pyle, J. A.,
875   Vaughn, B. H., Warwick, N. J., and White, J. W. C.: Very Strong Atmospheric Methane Growth in the 4 Years 2014–2017: Implications for the Paris Agreement, Global Biogeochemical Cycles, 33, 318–342, https://doi.org/10.1029/2018GB006009, 2019.

Oh, Y., Zhuang, Q., Liu, L., Welp, L. R., Lau, M. C. Y., Onstott, T. C., Medvigy, D., Bruhwiler, L., Dlugokencky, E. J., Hugelius, G., D'Imperio, L., and Elberling, B.: Reduced net methane emissions due to microbial methane oxidation in a warmer Arctic, Nature Climate Change, 10, 317–321, https://doi.org/10.1038/s41558-020-0734-z, number: 4 Publisher: Nature Publishing Group, 2020.

880   Pandey, S., Houweling, S., Krol, M., Aben, I., Monteil, G., Nechita-Banda, N., Dlugokencky, E. J., Detmers, R., Hasekamp, O., Xu, X., Riley, W. J., Poulter, B., Zhang, Z., McDonald, K. C., White, J. W. C., Bousquet, P., and Röckmann, T.: Enhanced methane emissions from tropical wetlands during the 2011 La Niña, Scientific Reports, 7, 45 759, https://doi.org/10.1038/srep45759, bandiera_abtest: a Cc_license_type: cc_by Cg_type: Nature Research Journals Number: 1 Primary_atype: Research Publisher: Nature Publishing

Group Subject_term: Atmospheric chemistry;Carbon cycle;Projection and prediction Subject_term_id: atmospheric-chemistry;carbon-cycle;projection-and-prediction, 2017.

Pandey, S., Gautam, R., Houweling, S., van der Gon, H. D., Sadavarte, P., Borsdorff, T., Hasekamp, O., Landgraf, J., Tol, P., van Kempen, T., Hoogeveen, R., van Hees, R., Hamburg, S. P., Maasakkers, J. D., and Aben, I.: Satellite observations reveal extreme methane leakage from a natural gas well blowout, Proceedings of the National Academy of Sciences, 116, 26 376–26 381, 2019.

Parker, R. J., Wilson, C., Bloom, A. A., Comyn-Platt, E., Hayman, G., McNorton, J., Boesch, H., and Chipperfield, M. P.: Exploring constraints on a wetland methane emission ensemble (WetCHARTs) using GOSAT observations, Biogeosciences, 17, 5669–5691, https://doi.org/10.5194/bg-17-5669-2020, publisher: Copernicus GmbH, 2020.

Quay, P. D., King, S. L., Stutsman, J., Wilbur, D. O., Steele, L. P., Fung, I., Gammon, R. H., Brown, T. A., Farwell, G. W., Grootes, P. M., and Schmidt, F. H.: Carbon isotopic composition of atmospheric CH4: Fossil and biomass burning source strengths, Global Biogeochemical Cycles, 5, 25–47, https://doi.org/10.1029/91GB00003, _eprint: https://agupubs.onlinelibrary.wiley.com/doi/pdf/10.1029/91GB00003, 1991.

Reeburgh, W. S., Hirsch, A. I., Sansone, F. J., Popp, B. N., and Rust, T. M.: Carbon kinetic isotope effect accompanying microbial oxidation of methane in boreal forest soils, Geochimica et Cosmochimica Acta, 61, 4761–4767, https://doi.org/10.1016/S0016-7037(97)00277-9, 1997.

Rohrer, F. and Berresheim, H.: Strong correlation between levels of tropospheric hydroxyl radicals and solar ultraviolet radiation, Nature, 442, 184–187, https://doi.org/10.1038/nature04924, number: 7099 Publisher: Nature Publishing Group, 2006.

Rosentreter, J. A., Borges, A. V., Deemer, B. R., Holgerson, M. A., Liu, S., Song, C., Melack, J., Raymond, P. A., Duarte, C. M., Allen, G. H., Olefeldt, D., Poulter, B., Battin, T. I., and Eyre, B. D.: Half of global methane emissions come from highly variable aquatic ecosystem sources, Nature Geoscience, 14, 225–230, https://doi.org/10.1038/s41561-021-00715-2, number: 4 Publisher: Nature Publishing Group, 2021.

Rowlinson, M. J., Rap, A., Arnold, S. R., Pope, R. J., Chipperfield, M. P., McNorton, J., Forster, P., Gordon, H., Pringle, K. J., Feng, W., Kerridge, B. J., Latter, B. L., and Siddans, R.: Impact of El Niño–Southern Oscillation on the interannual variability of methane and tropospheric ozone, Atmospheric Chemistry and Physics, 19, 8669–8686, https://doi.org/10.5194/acp-19-8669-2019, publisher: Copernicus GmbH, 2019.

Röckmann, T., Brass, M., Borchers, R., and Engel, A.: The isotopic composition of methane in the stratosphere: high-altitude balloon sample measurements, Atmospheric Chemistry and Physics, 11, 13 287–13 304, https://doi.org/10.5194/acp-11-13287-2011, 2011.

Saueressig, G., Crowley, J. N., Bergamaschi, P., Brühl, C., Brenninkmeijer, C. A. M., and Fischer, H.: Carbon 13 and D kinetic isotope effects in the reactions of CH4 with O(1D) and OH: New laboratory measurements and their implications for the isotopic composition of stratospheric methane, Journal of Geophysical Research: Atmospheres, 106, 23 127–23 138, https://doi.org/10.1029/2000JD000120, 2001.

Saunois, M., Stavert, A. R., Poulter, B., Bousquet, P., Canadell, J. G., Jackson, R. B., Raymond, P. A., Dlugokencky, E. J., Houweling, S., Patra, P. K., Ciais, P., Arora, V. K., Bastviken, D., Bergamaschi, P., Blake, D. R., Brailsford, G., Bruhwiler, L., Carlson, K. M., Carrol, M., Castaldi, S., Chandra, N., Crevoisier, C., Crill, P. M., Covey, K., Curry, C. L., Etiope, G., Frankenberg, C., Gedney, N., Hegglin, M. I., Höglund-Isaksson, L., Hugelius, G., Ishizawa, M., Ito, A., Janssens-Maenhout, G., Jensen, K. M., Joos, F., Kleinen, T., Krummel, P. B., Langenfelds, R. L., Laruelle, G. G., Liu, L., Machida, T., Maksyutov, S., McDonald, K. C., McNorton, J., Miller, P. A., Melton, J. R., Morino, I., Müller, J., Murguia-Flores, F., Naik, V., Niwa, Y., Noce, S., O'Doherty, S., Parker, R. J., Peng, C., Peng, S., Peters, G. P., Prigent, C., Prinn, R., Ramonet, M., Regnier, P., Riley, W. J., Rosentreter, J. A., Segers, A., Simpson, I. J., Shi, H., Smith, S. J.,

Steele, L. P., Thornton, B. F., Tian, H., Tohjima, Y., Tubiello, F. N., Tsuruta, A., Viovy, N., Voulgarakis, A., Weber, T. S., van Weele, M., van der Werf, G. R., Weiss, R. F., Worthy, D., Wunch, D., Yin, Y., Yoshida, Y., Zhang, W., Zhang, Z., Zhao, Y., Zheng, B., Zhu, Q., Zhu, Q., and Zhuang, Q.: The Global Methane Budget 2000–2017, 12, 1561–1623, https://doi.org/https://doi.org/10.5194/essd-12-1561-2020,
925   publisher: Copernicus GmbH, 2020.

Schwietzke, S., Sherwood, O. A., Bruhwiler, L. M. P., Miller, J. B., Etiope, G., Dlugokencky, E. J., Michel, S. E., Arling, V. A., Vaughn, B. H., White, J. W. C., and Tans, P. P.: Upward revision of global fossil fuel methane emissions based on isotope database, 538, 88–91, https://doi.org/10.1038/nature19797, 2016.

Sherwood, O. A., Schwietzke, S., Arling, V. A., and Etiope, G.: Global Inventory of Gas Geochemistry Data from Fossil Fuel, Microbial and
930   Burning Sources, version 2017, Earth System Science Data, 9, 639–656, https://doi.org/https://doi.org/10.5194/essd-9-639-2017, 2017.

Snover, A. K. and Quay, P. D.: Hydrogen and carbon kinetic isotope effects during soil uptake of atmospheric methane, Global Biogeochemical Cycles, 14, 25–39, https://doi.org/10.1029/1999GB900089, 2000.

Spahni, R., Wania, R., Neef, L., van Weele, M., Pison, I., Bousquet, P., Frankenberg, C., Foster, P. N., Joos, F., Prentice, I. C., and van Velthoven, P.: Constraining global methane emissions and uptake by ecosystems, Biogeosciences, 8, 1643–1665,
935   https://doi.org/10.5194/bg-8-1643-2011, publisher: Copernicus GmbH, 2011.

Spivakovsky, C. M., Logan, J. A., Montzka, S. A., Balkanski, Y. J., Foreman-Fowler, M., Jones, D. B. A., Horowitz, L. W., Fusco, A. C., Brenninkmeijer, C. a. M., Prather, M. J., Wofsy, S. C., and McElroy, M. B.: Three-dimensional climatological distribution of tropospheric OH: Update and evaluation, Journal of Geophysical Research: Atmospheres, 105, 8931–8980, https://doi.org/10.1029/1999JD901006, 2000.

940 Still, C. J., Berry, J. A., Collatz, G. J., and DeFries, R. S.: Global distribution of C3 and C4 vegetation: Carbon cycle implications, Global Biogeochemical Cycles, 17, 6–1–6–14, https://doi.org/https://doi.org/10.1029/2001GB001807, _eprint: https://agupubs.onlinelibrary.wiley.com/doi/pdf/10.1029/2001GB001807, 2003.

Tenkanen, M., Tsuruta, A., Rautiainen, K., Kangasaho, V., Ellul, R., and Aalto, T.: Utilizing Atmospheric Concentrations and Earth Observations of Soil Freeze/Thaw data to Estimate Cold Season Methane Emissions in the Northern Hemisphere, Remote Sensing, to be
945   submitted, 2021.

Thompson, R. L., Sasakawa, M., Machida, T., Aalto, T., Worthy, D., Lavric, J. V., Lund Myhre, C., and Stohl, A.: Methane fluxes in the high northern latitudes for 2005–2013 estimated using a Bayesian atmospheric inversion, Atmospheric Chemistry and Physics, 17, 3553–3572, https://doi.org/10.5194/acp-17-3553-2017, publisher: Copernicus GmbH, 2017.

Thompson, R. L., Nisbet, E. G., Pisso, I., Stohl, A., Blake, D., Dlugokencky, E. J., Helmig, D., and White, J. W. C.: Variability in Atmospheric
950   Methane From Fossil Fuel and Microbial Sources Over the Last Three Decades, Geophysical Research Letters, 45, 11,499–11,508, https://doi.org/10.1029/2018GL078127, 2018.

Thoning, K. W., Tans, P. P., and Komhyr, W. D.: Atmospheric carbon dioxide at Mauna Loa Observatory: 2. Analysis of the NOAA GMCC data, 1974–1985, Journal of Geophysical Research: Atmospheres, 94, 8549–8565, https://doi.org/10.1029/JD094iD06p08549, _eprint: https://onlinelibrary.wiley.com/doi/pdf/10.1029/JD094iD06p08549, 1989.

955 Tsuruta, A., Aalto, T., Backman, L., Hakkarainen, J., Laan-Luijkx, I. T. v. d., Krol, M. C., Spahni, R., Houweling, S., Laine, M., Dlugokencky, E., Gomez-Pelaez, A. J., Schoot, M. v. d., Langenfelds, R., Ellul, R., Arduini, J., Apadula, F., Gerbig, C., Feist, D. G., Kivi, R., Yoshida, Y., and Peters, W.: Global methane emission estimates for 2000–2012 from CarbonTracker Europe-CH$_4$ v1.0, Geoscientific Model Development, 10, 1261–1289, https://doi.org/doi:10.5194/gmd-10-1261-2017, 2017.

Tsuruta, A., Aalto, T., Backman, L., Krol, M. C., Peters, W., Lienert, S., Joos, F., Miller, P. A., Zhang, W., Laurila, T., Hatakka, J., Leskinen,
960   A., Lehtinen, K. E. J., Peltola, O., Vesala, T., Levula, J., Dlugokencky, E., Heimann, M., Kozlova, E., Aurela, M., Lohila, A., Kauhaniemi,
        M., and Gomez-Pelaez, A. J.: Methane budget estimates in Finland from the CarbonTracker Europe-CH4 data assimilation system, Tel-
        lus B: Chemical and Physical Meteorology, 71, 1565 030, https://doi.org/10.1080/16000889.2018.1565030, publisher: Taylor & Francis
        _eprint: https://doi.org/10.1080/16000889.2018.1565030, 2019.

Tunnicliffe, R. L., Ganesan, A. L., Parker, R. J., Boesch, H., Gedney, N., Poulter, B., Zhang, Z., Lavrič, J. V., Walter, D., Rigby, M., Henne,
965   S., Young, D., and O'Doherty, S.: Quantifying sources of Brazil's CH_4 emissions between 2010 and 2018 from satellite data, Atmospheric
        Chemistry and Physics, 20, 13 041–13 067, https://doi.org/10.5194/acp-20-13041-2020, publisher: Copernicus GmbH, 2020.

Turner, A. J., Frankenberg, C., and Kort, E. A.: Interpreting contemporary trends in atmospheric methane, Proceedings of the National
        Academy of Sciences, 116, 2805–2813, https://doi.org/10.1073/pnas.1814297116, publisher: National Academy of Sciences Section:
        Perspective, 2019.

970   Tyler, S. C., Brailsford, G. W., Yagi, K., Minami, K., and Cicerone, R. J.: Seasonal variations in methane flux andδl3CH4 values for rice pad-
        dies in Japan and their implications, Global Biogeochemical Cycles, 8, 1–12, https://doi.org/https://doi.org/10.1029/93GB03123, _eprint:
        https://onlinelibrary.wiley.com/doi/pdf/10.1029/93GB03123, 1994a.

Tyler, S. C., Crill, P. M., and Brailsford, G. W.: 13C12C Fractionation of methane during oxidation in a temperate forested soil, Geochimica
        et Cosmochimica Acta, 58, 1625–1633, https://doi.org/10.1016/0016-7037(94)90564-9, 1994b.

975   Tyler, S. C., Rice, A. L., and Ajie, H. O.: Stable isotope ratios in atmospheric CH_4: Implications for seasonal
        sources and sinks, Journal of Geophysical Research: Atmospheres, 112, https://doi.org/10.1029/2006JD007231, _eprint:
        https://agupubs.onlinelibrary.wiley.com/doi/pdf/10.1029/2006JD007231, 2007.

Ulyatt, M. J., Lassey, K. R., Shelton, I. D., and Walker, C. F.: Seasonal variation in methane emission from dairy cows and breed-
        ing ewes grazing ryegrass/white clover pasture in New Zealand, New Zealand Journal of Agricultural Research, 45, 217–226,
980   https://doi.org/10.1080/00288233.2002.9513512, publisher: Taylor & Francis _eprint: https://doi.org/10.1080/00288233.2002.9513512,
        2002.

VanderZaag, A., Flesch, T., Desjardins, R., Baldé, H., and Wright, T.: Measuring methane emissions from two dairy farms: Seasonal and
        manure-management effects, Agricultural and Forest Meteorology, 194, 259–267, https://doi.org/10.1016/j.agrformet.2014.02.003, 2014.

Villarreal, S. and Vargas, R.: Representativeness of FLUXNET Sites Across Latin America, Journal of Geo-
985   physical Research: Biogeosciences, 126, e2020JG006 090, https://doi.org/10.1029/2020JG006090, _eprint:
        https://agupubs.onlinelibrary.wiley.com/doi/pdf/10.1029/2020JG006090, 2021.

Wang, X., Jacob, D. J., Eastham, S. D., Sulprizio, M. P., Zhu, L., Chen, Q., Alexander, B., Sherwen, T., Evans, M. J., Lee, B. H., Haskins,
        J. D., Lopez-Hilfiker, F. D., Thornton, J. A., Huey, G. L., and Liao, H.: The role of chlorine in global tropospheric chemistry, Atmospheric
        Chemistry and Physics, 19, 3981–4003, https://doi.org/10.5194/acp-19-3981-2019, publisher: Copernicus GmbH, 2019.

990   Warwick, N. J., Cain, M. L., Fisher, R., France, J. L., Lowry, D., Michel, S. E., Nisbet, E. G., Vaughn, B. H., White, J. W. C., and Pyle,
        J. A.: Using δ^{13}C-CH$_4$ and δD-CH$_4$ to constrain Arctic methane emissions, Atmospheric Chemistry and Physics, 16, 14 891–14 908,
        https://doi.org/https://doi.org/10.5194/acp-16-14891-2016, 2016.

Whiticar, M., Faber, E., and Schoell, M.: Biogenic methane formation in marine and freshwater environments: CO2 reduction vs. acetate
        fermentation—Isotope evidence, Geochimica et Cosmochimica Acta, 50, 693–709, https://doi.org/10.1016/0016-7037(86)90346-7, 1986.

995   Xu, X., Riley, W. J., Koven, C. D., Billesbach, D. P., Chang, R. Y.-W., Commane, R., Euskirchen, E. S., Hartery, S., Harazono, Y., Iwata, H.,
        McDonald, K. C., Miller, C. E., Oechel, W. C., Poulter, B., Raz-Yaseef, N., Sweeney, C., Torn, M., Wofsy, S. C., Zhang, Z., and Zona, D.:

Atmospheric
Chemistry
and Physics
Discussions

A multi-scale comparison of modeled and observed seasonal methane emissions in northern wetlands, Biogeosciences, 13, 5043–5056, https://doi.org/10.5194/bg-13-5043-2016, publisher: Copernicus GmbH, 2016.

Yan, X., Akiyama, H., Yagi, K., and Akimoto, H.: Global estimations of the inventory and mitigation potential of methane emissions from rice cultivation conducted using the 2006 Intergovernmental Panel on Climate Change Guidelines, Global Biogeochemical Cycles, 23, https://doi.org/10.1029/2008GB003299, _eprint: https://agupubs.onlinelibrary.wiley.com/doi/pdf/10.1029/2008GB003299, 2009.

Zazzeri, G., Lowry, D., Fisher, R. E., France, J. L., Lanoisellé, M., Kelly, B. F. J., Necki, J. M., Iverach, C. P., Ginty, E., Zimnoch, M., Jasek, A., and Nisbet, E. G.: Carbon isotopic signature of coal-derived methane emissions to the atmosphere: from coalification to alteration, Atmospheric Chemistry and Physics, 16, 13 669–13 680, https://doi.org/10.5194/acp-16-13669-2016, publisher: Copernicus GmbH, 2016.

Zhang, B., Tian, H., Ren, W., Tao, B., Lu, C., Yang, J., Banger, K., and Pan, S.: Methane emissions from global rice fields: Magnitude, spatiotemporal patterns, and environmental controls, Global Biogeochemical Cycles, 30, 1246–1263, https://doi.org/10.1002/2016GB005381, _eprint: https://agupubs.onlinelibrary.wiley.com/doi/pdf/10.1002/2016GB005381, 2016.

Zhang, G., Ma, J., Yang, Y., Yu, H., Shi, Y., and Xu, H.: Variations of Stable Carbon Isotopes of CH4 Emission from Three Typical Rice Fields in China, Pedosphere, 27, 52–64, https://doi.org/10.1016/S1002-0160(15)60096-0, 2017.

Zhang, Y., Jacob, D. J., Lu, X., Maasakkers, J. D., Scarpelli, T. R., Sheng, J.-X., Shen, L., Qu, Z., Sulprizio, M. P., Chang, J., Bloom, A. A., Ma, S., Worden, J., Parker, R. J., and Boesch, H.: Attribution of the accelerating increase in atmospheric methane during 2010–2018 by inverse analysis of GOSAT observations, Atmospheric Chemistry and Physics, 21, 3643–3666, https://doi.org/10.5194/acp-21-3643-2021, publisher: Copernicus GmbH, 2021.

Zhao, Y., Saunois, M., Bousquet, P., Lin, X., Berchet, A., Hegglin, M. I., Canadell, J. G., Jackson, R. B., Hauglustaine, D. A., Szopa, S., Stavert, A. R., Abraham, N. L., Archibald, A. T., Bekki, S., Deushi, M., Jöckel, P., Josse, B., Kinnison, D., Kirner, O., Marécal, V., O'Connor, F. M., Plummer, D. A., Revell, L. E., Rozanov, E., Stenke, A., Strode, S., Tilmes, S., Dlugokencky, E. J., and Zheng, B.: Intermodel comparison of global hydroxyl radical (OH) distributions and their impact on atmospheric methane over the 2000–2016 period, Atmospheric Chemistry and Physics, 19, 13 701–13 723, https://doi.org/10.5194/acp-19-13701-2019, publisher: Copernicus GmbH, 2019.

Zhu, Q., Peng, C., Ciais, P., Jiang, H., Liu, J., Bousquet, P., Li, S., Chang, J., Fang, X., Zhou, X., Chen, H., Liu, S., Lin, G., Gong, P., Wang, M., Wang, H., Xiang, W., and Chen, J.: Interannual variation in methane emissions from tropical wetlands triggered by repeated El Niño Southern Oscillation, Global Change Biology, 23, 4706–4716, https://doi.org/10.1111/gcb.13726, _eprint: https://onlinelibrary.wiley.com/doi/pdf/10.1111/gcb.13726, 2017.